Imbalanced mitochondrial dynamics contributes to the pathogenesis of X-linked adrenoleukodystrophy.

Nathalie Launay[1,2,†], Jone Lopez-Erauskin[1,3,†], Patrizia Bianchi[1,4], Sanjib Guha[1,5], Janani Parameswaran[1,6], Andrea Coppa[1], Lorenzo Torreni[1,7,] Agatha Schlüter[1,2], Stéphane Fourcade[1,2], Abraham J. Paredes-Fuentes[8], Rafael Artuch[2,9], Carlos Casasnovas[1,2,10], Montserrat Ruiz[1,2] and Aurora Pujol[1,2,11]*.

[†] **These authors contributed equally**

Abstract

The peroxisomal disease adrenoleukodystrophy (X-ALD) is caused by loss of the transporter of very-long-chain fatty acids (VLCFAs), ABCD1. An excess of these VLCFAs impacts homeostatic functions pivotal for axonal maintenance, i.e., redox metabolism, glycolysis, and mitochondrial respiration. As mitochondrial function and morphology are intertwined, we set out to investigate the role of mitochondrial dynamics in X-ALD models. We used quantitative 3D transmission electron microscopy to unveil mitochondrial fragmentation in corticospinal axons in *Abcd1*$^{-}$ mice. In patient fibroblasts, excess VLCFA triggers mitochondrial fragmentation through the phosphorylation of DRP1 (DRP1^{S616}) in a redox-dependent manner. Blockade of DRP1-driven fission with the peptide P110 preserves mitochondrial morphology. Furthermore, mRNA inhibition of DRP1 prevents mitochondrial fragmentation and protects axonal health in a *C. elegans* model of X-ALD, underscoring DRP1 as a potential therapeutic target. Elevated levels of circulating cell-free mtDNA (ccfmtDNA) in patients' cerebrospinal fluid align this leukodystrophy with primary mitochondrial disorders.

Author affiliations:

1. Neurometabolic Diseases Laboratory, Institute of Neuropathology, IDIBELL, 08908 L'Hospitalet de Llobregat, Barcelona, Spain, EU.

2. CIBERER, Centro de Investigación Biomédica en Red de Enfermedades Raras, ISCIII, Madrid, Spain, EU.
3. Ludwig Institute for Cancer Research, University of California at San Diego, La Jolla, CA 92093, USA.
4. Institut de Neurociències and Department of Cell Biology, Physiology and Immunology, Facultat de Medicina, Universitat Autònoma de Barcelona, Bellaterra, Spain, EU.
5. University of Rochester, Department of Anesthesiology & Perioperative Medicine, 6 Rochester, NY, USA.
6. Department of Cell Biology, Emory University, Atlanta, GA 30322, USA.
7. Programa de Doctorat en Biomedicina, Universitat de Barcelona, Barcelona, Spain.
8. Division of Inborn Errors of Metabolism-IBC, Biochemistry and Molecular Genetics Department, Hospital Clínic de Barcelona, 08028 Barcelona, Spain.
9. Clinical Biochemistry Department, Institut de Recerca Sant Joan de Déu, Hospital Sant Joan de Déu, Barcelona, Spain, EU.
10. Neuromuscular Unit, Neurology Department, Bellvitge University Hospital, Universitat de Barcelona, Barcelona, Spain, EU.
11. Catalan Institution of Research and Advanced Studies (ICREA), Barcelona, Spain, EU.

Correspondence to: Aurora Pujol

Neurometabolic Diseases Laboratory
Institut de Neuropatologia de Bellvitge, IDIBELL
Gran Via, 199
08908 L'Hospitalet de Llobregat
Barcelona, Spain
apujol@idibell.cat
Tel: (+34) 932 60 71 37
Fax: (+34) 932 60 74 14

Running title: Mitochondria-peroxisomal cross-talk in X-ALD

Keywords: Mitochondrial dynamics; DRP1; X-ALD; VLCFA**;** ccfmtDNA; P110

Introduction

Mitochondria are multifaceted organelles essential for ATP production, Ca^{2+} homeostasis, programmed cell death regulation, and reactive oxygen species (ROS) generation. [1] The functions of mitochondria have been intimately linked to their morphology, which is shaped by ongoing fusion and fission events. An imbalance in mitochondrial dynamics toward fission causes mitochondrial fragmentation, leading to mitochondrial bioenergetic failure, which is associated with aging as well metabolic and neurodegenerative diseases. [2,3,4,5] Mitochondria are particularly important in neurons to satisfy the energy needs of electrical excitability and synaptic functions. To this end, healthy neurons precisely regulate mitochondrial dynamics to transport mitochondria to distal locations, including synapses, dendrites, and axons. [6,7]

In this study, we investigated whether mitochondrial dynamics are altered in the peroxisomal disease adrenoleukodystrophy (X-ALD, OMIM #300100) and the extent to which this impairment contributes to disease pathophysiology. X-ALD is the most common leukodystrophy, with an incidence of 1:14700 live births. [8,9] X-ALD is characterized by a striking variation in clinical symptoms, even within the same family. The two main neurological phenotypes include (i) cALD or cAMN, a rapidly progressing cerebral demyelinating leukodystrophy that leads to death (35-40% of cases), and (ii) slowly progressing adult-onset adrenomyeloneuropathy (AMN), which makes up 60% of cases and affects adults and is characterized by distal axonopathy of corticospinal tracts, thereby leading to spastic paraparesis with frequent peripheral neuropathy and adrenal insufficiency. Women may be mildly affected. [8,10-12] All patients with X-ALD have mutations in the *ABCD1* gene located on Xq28, which encodes the adrenoleukodystrophy protein (ALDP or ABCD1) responsible for the import of very long-chain fatty acids (VLCFA; C≥22:0) into peroxisomes for β-oxidation. Consequently, VLCFAs, especially hexacosanoic acid (C26:0), accumulate in patient tissues and plasma and constitute well-established diagnostic biomarkers that are also useful for newborn screening. [9,13,14] The mouse model of X-ALD (*Abcd1*-) develops a late-onset axonopathy and thus resembles AMN, the most frequent X-ALD phenotype. [15,16] We previously identified oxidative damage, altered mitochondrial respiration and decreased mitochondrial biogenesis and bioenergetic dysfunction as early contributing factors to axonal degeneration in Abcd1-

null spinal cords. [17-22] *Abcd1*$^{-}$ mice exhibit accumulation of oxidatively modified proteins, mostly proteins involved in glycolysis, the Krebs cycle and mitochondrial oxidative phosphorylation (OXPHOS) in the spinal cord. [20,23] Moreover, we found that mitochondria are the main source of ROS in X-ALD fibroblasts when cells are exposed to an excess of C26:0. [24] However, the mechanisms involved in the interaction of accumulated VLCFAs with the mitochondrial network and dynamics and the subsequent excessive ROS production derived from the organelle remain unclear.

Here, we provide evidence that the accumulation of VLCFAs in fibroblasts increases the phosphorylated form of DRP1^{S616}, inducing an imbalance in mitochondrial dynamics toward fission. This provokes the excessive production of ROS by dysfunctional fragmented mitochondria, triggering mitochondrial failure as a major contributor to axonal degeneration in X-ALD models.

Materials and Methods

Animals

Mice

Generation and genotyping of *Abcd1*$^{-}$ mice have been previously described. [15,16,25] *Abcd1*$^{-}$ mice are viable and exhibit a phenotype resembling the late-onset axonal degeneration in spinal cords presented by most AMN patients, characterized by spastic paraparesis due to degeneration of the corticospinal tract but without signs of active inflammatory demyelination in the brain.

Mice were maintained on the C57BL/6J genetic background in our animal facility, housed under a 12-hour light/dark cycle and fed a regular diet *ad libitum*. *Abcd1*$^{-}$ and wild-type mice were separated into control and treated groups. Treated groups were fed a mixture of antioxidants that included 1000 IU/kg Trolox (Cat: 238813, Merck) and 0.5% α-lipoic acid (Cat: T1395, Merck) in the diet and 1% NAC (Cat: A7250, Merck) in water. Daily feedings were initiated at 8 months of age and were continued for 4 months until sacrifice. Animals were sacrificed, and tissues were recovered and stored at −80 °C.

All methods employed in this study were in accordance with the Guide for the Care and Use of Laboratory Animals published by the US National Institutes of Health (NIH

publication No. 85-23, revised 1996) and the Ethics Committees of IDIBELL and the Generalitat de Catalunya.

C. elegans strains

All the strains used were provided by the *Caenorhabditis* Genetic Center (CGC) unless otherwise indicated. N2 (Bristol) was used as the WT strain (N2). The partial deletion strain RB675, *pmp-4(ok396),* was backcrossed 10 times into the N2 strain prior to experimental work. All the strains mentioned in the manuscript are detailed in Supplementary Table 1.

Maintenance, crosses, and other genetic manipulations were all performed via standard procedures (http://www.wormbook.org). Worm strains were grown at 20 °C on nematode growth medium (NGM) plates seeded with OP50 Escherichia coli.

Primary human fibroblasts and cell culture conditions

Primary human fibroblasts were collected from healthy individuals and AMN patients according to the IDIBELL guidelines for sampling, including informed consent from the persons involved or their representatives. Fibroblasts were prepared from skin biopsies.

Primary human fibroblasts were cultivated in Dulbecco's modified Eagle's medium (containing 10% fetal bovine serum, 100 U/ml penicillin and 100 µg streptomycin) at 37 °C in humidified 5% CO_2/95% air. Unless otherwise stated, experiments were carried out with cells at 80% confluence. Skin biopsies to prepare fibroblasts were collected according to the institutional guidelines for sampling, including informed consent from the subjects involved or their representatives.

Cells were treated with either single doses of C26:0 (50 µM, Cat: H0388, Merck), NAC (1 mM) or P110 (1 µM, Cat: 6897/1, R&D systems). Ethanol and TAT (Cat: H0292, Merck) were used as vehicle controls for C26:0 and P110, respectively. NAC was dissolved in water.

Cerebrospinal fluid collection

CSF was obtained by lumbar puncture from healthy individuals and AMN patients according to the IDIBELL guidelines for sampling, including informed consent from the persons involved or their representatives. CSF was centrifuged (2.000 g, 4° C, 10 min) to collect the clear supernatant, which was aliquoted and immediately stored at -80° C. Control samples (age range: 0.02–34 years old) were collected at the Emergency Department of the Hospital Infantil Sant Joan de Déu (Barcelona) mainly because of suspicion of meningitis and encephalitis. An aliquot was used for routine biochemical measurements, cell counts, and microbiological investigations. The remaining volume was centrifuged (2.000 g, 4 °C, 10 min) to collect the clear supernatant, which was aliquoted and immediately stored at -80 °C at the Biobanc de l'Hospital Infantil Sant Joan de Déu until further analysis. The exclusion criteria were the presence of viral or bacterial meningitis, traumatic or tumoral disorders of the CNS, intracerebral hemorrhage, CSF blood contamination, and pleocytosis. AMN samples and adult controls were collected at the Bellvitge University Hospital (Barcelona) from patients participating in different clinical trials and consented family members (Clinical Research Ethics Committee of Bellvitge approval number: PR328/20)

Reverse transcription (RT)-PCR analysis

Total RNA was isolated from homogenized spinal cords using the RNeasy Mini Kit (Quiagen) according to the manufacturer's instructions. Next, first-strand cDNA was synthesized for each RNA sample using Superscript II reverse transcriptase (Cat: 18064022, Invitrogen) and oligo-dT. Expression levels of the candidate proteasome genes were analyzed through RT–PCR using TaqMan®Gene Expression Assays. The expression levels were relatively quantified using the 'Delta–Delta Ct' (ΔΔCt) method with *RPL0* as an endogenous control. Transcript quantification was performed in duplicate for each sample. [26]

Immunofluorescence

Spinal cords from 12-month-old wild-type and *Abcd1* mice were embedded in paraffin, and serial sections (4 µm thick) were cut in a transverse or longitudinal (1 cm long) plane after perfusion with 4% paraformaldehyde as previously described. [16,27-29] Spinal cords

were incubated with NeuN (1:100, Cat: ab17748, Abcam) and phospho-DRP1^{S616} (1:200, Cat: 3455, Cell signaling technology) antibodies overnight at 4 °C and then finally incubated with fluorescence-conjugated secondary antibodies (Anti-rabbit Alexa-fluor 555, 1:1000, Cat: A-21428, Thermo Fisher; Anti-mouse Alexa-fluor 488, 1:1000, Cat: A-11001, Thermo Fisher for 1 h at 25 °C.

For the fibroblast study, immunofluorescence was performed as previously described. [26] Briefly, cells were stained with Mitotracker™ (Cat: M7510, Thermo Fisher) and fixed with 3.7% paraformaldehyde and 5% sucrose, incubated in blocking buffer (1% BSA, 0.2% powdered milk, 2% NCS, 0.1 M glycine, 0.1% Triton-X-100) for 15 min at 25 °C, incubated with anti-phospho DRP1^{S616} antibody (1:200, Cat: 3455, Cell signaling technology) overnight at 4 °C, and then incubated with fluorescence-conjugated secondary antibody (Anti-mouse Alexa-fluor 488, 1:1000, Cat: A-11001, Thermo Fisher) for 1 h at room temperature (RT).

Confocal images were acquired using a Leica TCS SL laser scanning confocal spectral microscope (Leica Microsystems Heidelberg GmbH, Mannheim, Germany), and images were analyzed with ImageJ software.

Western blot

Spinal cord tissues and human fibroblasts were lysed in ice-cold RIPA buffer (50 mM Tris-HCl, pH 8, 12 mM deoxycholic acid, 150 mM NaCl and 1% NP40, supplemented with Complete Protease Inhibitor Cocktail (Cat: 11697498001, Merck/Roche) and Phosphatase Inhibitor Cocktail (PhosStop, Cat: 4906845001, Merck/roche) using a Teflon-on-glass homogenizer and then centrifuged at 1500 x g for 10 min at 4 °C. The protein concentration was determined using a BCA protein assay kit (Thermo Fisher). Samples were boiled for 5 min in Laemmli's buffer and run on Bis-tris gels. After electrophoresis, proteins were transferred to nitrocellulose membranes using the iBlot® 2 Dry blotting system (Life Technologies) and then incubated with appropriate antibodies. The following antibodies were used in the experiments: anti-DRP1 (Cat: 611739, BD Biosciences), anti-phospho-DRP1^{S616} (Cat: 3455, Cell signaling technology), anti-phospho-DRP1^{S637} (Cat: 6319, Cell signaling technology), anti-MFN1 (Cat: 13798-1AP, Proteintech), anti-MFN2 (Cat: M6444, Merck), anti-OPA1 (Cat: 612607, BD transduction laboratories), anti-VDAC (Cat: ab96140, Abcam), anti-γ-Tubulin

(Cat:T6557, Merck), Anti- mouse IgG linked to Horseradish peroxidase (Cat: P0447, Dakocytomation) and Anti- rabbit IgG linked to Horseradish peroxidase (Cat: P0448, Dakocytomation).

Proteins were visualized with the Amersham ECL Western blotting detection system (GE Healthcar bio-sciences AB), followed by exposure to CL-XPosure Film (Thermo Scientific). For all quantification of band intensities, Quantity One 1-D analysis software was used.

Mitochondrial isolation

Fresh spinal cord was homogenized in sucrose buffer (sucrose 0.32 M, HEPES 4 mM pH 7.4 and protease inhibitor cocktail) using a Dounce homogenizer with a tight pestle and then centrifuged for 10 min (1000*g*). The supernatant (S1a) was kept on ice, and the pellet was resuspended in ice-cold sucrose buffer and then centrifuged for 10 min (1000*g*). The supernatant (S1b) was kept on ice, and the pellet was resuspended in ice-cold sucrose buffer and centrifuged for 10 min (1000*g*). The supernatant (S1c) was kept on ice, and the pellet was discarded. The supernatants S1a, S1b and S1c were centrifuged (16 000*g*) for 10 min. The pellet contained the mitochondrial-enriched fractions. Mitochondrial fractions were checked by western blotting with antibodies against the mitochondrial marker VDAC.

Analysis of mitochondrial morphology in fibroblasts

Mitochondria were stained using MitoTracker™, and confocal images were acquired using a Leica TCS SL laser scanning confocal spectral microscope. Then, images were processed using ImageJ Software. An original stack of mitochondria following 3-D filtering and reconstruction was mapped into a single grayscale image and thresholded. Then, mitochondrial morphological types were classified according to criteria and methods previously described. [30-33] Mitochondria subtypes were scored by using the Analyze Particle function of ImageJ software. Circularity=1.0 indicates a perfect circle, while a value approaching zero indicates an elongated shape. The inverse of mitochondrial circularity (1/circularity) was used as an indicator of mitochondrial elongation. [34]

Small globules, donuts or small globules were selected and measured manually using freeform drawing tools to avoid mismatch. To generate the mitochondrial color map, each mitochondrion was stained following a color code (green- long linear tubules, light blue- short linear tubules, dark blue- fragmented, small globules, red- donuts and cyan- small-globules). For quantitative analysis, the proportion of each mitochondria type was expressed as a percentage relative to the total mitochondrial area per cell.

3D EM reconstruction using serial block-face scanning electron microscopy (SBFSEM)

3D EM reconstruction was performed in 5 male mice from each genotype (*Wt* and *Abcd1*$^{-}$) at 12 months of age. Block face EM images were acquired through Renovo neural EM services (Cleveland, OH) using a Zeiss Sigma VP scanning electron microscope. Tissues were prepared according to company directions. Briefly, mice were perfused with glutaraldehyde 2.5% and paraformaldehyde 4% in 0.1 M sodium cacodylate buffer and stored in perfusion solution. Tissue processing and embedding were performed by Renovo. Sections were imaged at a resolution of 8 nm/pixel with a section thickness of 80 nm/slice. Confocal microscopy was performed using an Olympus Fluoview or Olympus DSU spinning disk microscope. Axons, synapses and mitochondria were segmented in each slice by manual segmentation using Reconstruct software. [35] Synaptic terminals were identified by the presence of synaptic vesicles and a close apposition of the postsynaptic membrane.

RNAi experiments

RNAi experiments were performed as previously described. [36] The *drp-1* bacterial RNAi feeding construct was obtained from the Ahringer *C. elegans* library (Source Bioscience, Nottingham, UK) and grown overnight in Luria broth (LB) media containing 100 µg/ml ampicillin. Nematode growth medium (NGM) plates containing 1 µM IPTG were seeded with 200 µl of RNAi culture and allowed to dry overnight. For the analysis of the effect of *drp-1* on mitochondrial morphology and axonal integrity, 10 L1-stage worms Prgef-1::mito::gfp, *Punc-25::gfp* or *Pmec-7::gfp* were transferred to NGM plates and grown at 20 °C until adulthood. Adult worms were then transferred to corresponding freshly made

RNAi plates (empty vector (*EV*) and *drp-1* RNAi) and allowed to lay eggs for 6 h to synchronize. Worms were transferred every two days to new plates. Mitochondrial size and axonal damage were analyzed on Day 7 of development (L4+7 days).

Analysis of GABAergic and mechanosensory neuron–associated abnormalities

Worms were grown at 20 °C for at least two generations before the experiments. Animal age refers to the adult age measured in days, calculated by adding one day consecutively from the given animal that went through L4. [37] The animals were transferred daily to avoid mixing populations, and the animals were considered dead when they stopped exhibiting pharyngeal pumping and failed to respond to mild touch with a platinum wire picker. After synchronization, F1 hermaphrodite animals were maintained at 20 °C until the late L4 larval stage and then transferred to the final assay plates (50 worms/plate).

For imaging, Day 7 animals (7 days after larval stage 4) were mounted by placing them in 6% agarose pads on glass slides, immobilized with 10 mM sodium azide on 6% agar pads and subsequently mounted for image analysis. All images were acquired under the same exposure conditions with a 20x objective, and for each experimental replicate, all genotypes were represented and imaged that day.

The worms were scored for the number of GABAergic neurons, gaps in the ventral cord, gaps in the dorsal cord and defects in axonal morphology. [38,39] The formula used to quantify axonal damage was as follows: % of axonal damage = [((number of commissural abnormalities + number of gaps/animal)/number of axons detected) x100].

For analysis of touch neurons, *Pmec-7:: gfp*-expressing animals scored positive for the presence of extraneuronal processes when a visible GFP-labeled branch emanating from the posterior portion of the ALM cell body was observed. Similarly, ALM/PLM neuron pairs were scored as overextension defects when the PLM neurite extended anterior to the ALM cell body. Other defects in axonal morphology (specifically in the PLM neuron) were assigned to one of the following classes of neuronal abnormality: broken or gap in the axon structure, blebbed or bead-like structure on the axon body, or misguided or wavy shaped axon.

All experiments were performed blindly and by different investigators to guarantee the reliability of the obtained measurements.

CcfmtDNA copy number

CcfmtDNA copy number was calculated by ddPCR according to the method described by Trifunov et al. [40] The 20 mL reactions consisted of 5 mL of CSF samples, 1X ddPCR supermix for probes (no dUTP), 250 nmol/L ND1 probe, 500 nmol/L ND1 primers, 125 nmol/L ND4 (or B2M or BAX) probe, 250 nmol/L ND4 (or B2M or BAX) primers, and nuclease-free water, as previously reported. [41,42] Reactions were transferred to ddPCR 96-well plates. Droplet generation was carried out manually using a QXDx droplet generator. For this purpose, 70 µL of droplet generation oil was added to each sample, and DG8 cartridges and DG8 gaskets were used for the QX200/QX100 droplet generator. Droplets were transferred to 96-well plates and then sealed for amplification. PCRs were carried out in a C1000 touch thermal cycler using standard cycling conditions: 95 °C for 10 min, 40 cycles of 94 °C for 30 s and 60 °C for 1 min, and then 98 °C for 10 min. Following PCR amplification, droplets were read on a QX200 droplet reader, and ddPCR data were analyzed using QuantaSoft software. All Primers and probes used for ddPCR are detailed in Supplementary Table 2.

All experiments were performed at least in duplicate, and each sample was assessed at least in triplicate. Only samples that exhibited more than 10 000 droplets were included in the analysis.

Data analysis and statistics

Statistical significance was assessed using Student's *t* test whenever two groups were compared. When analyzing multiple groups, we used one-way ANOVA and Tukey's *post hoc* test to determine statistical significance. Statistical analysis of axonal mitochondrial morphology in the Abcd1^{-} mouse model was performed by the Wilcoxon rank sum test according to the Shapiro–Wilk normality test. Statistical analysis of mechanosensory neurons in the *C. elegans* model was performed by Fisher's exact test. All the data are presented as the mean± SD (*, $P < 0.05$; **, $P < 0.01$; ***, $P < 0.001$).

Data availability

The authors confirm that the data supporting the findings of this study are available within the article and its Supplementary material. Derived data supporting the findings of this study are available from the corresponding author on request.

Results

Mitochondrial length is decreased in axons of the *Abcd1*$^{-}$ mouse spinal cord

The *Abcd1*$^{-}$ mice showed slower motor nerve conduction and locomotor disability signs in rotarod, treadmill, bar-cross, and clasping tests by 20 months. [17] In this model, axonopathy is mainly observed in the motor corticospinal tracts from 16 months of age and is characterized by the occurrence of irregular myelin sheaths and collapsed axons. [12,15,43] We set out to study the morphology of the mitochondrial network by morphometric analysis of 3D-reconstructed electron microscopy images of axonal mitochondria of *Abcd1*$^{-}$ mice at 14 months compared to the axonal mitochondria in *Wt* mice at the same age. Comparison between *Wt* and *Abcd1*$^{-}$ mouse motor corticospinal tracks revealed shorter mitochondria (Fig. 1A and B) with reduced volume (Fig. 1C and D) and smaller size inside the large caliber myelinated axons (size is inversely proportional to the Sa/V ratio) (Fig. 1E). We defined large caliber axons as those with volumes ≥ 40 µm³. We also investigated medium- and small-caliber myelinated axons, the latter with a volume ≤ 10 µm³ (Supplementary Fig. 1). The smaller-caliber axons also showed reduced mitochondrial length (Supplementary Fig. 1B), volume (Supplementary Fig. 1C) and size (Supplementary Fig. 1D) compared to *Wt* littermates.

Altered mitochondrial morphology in presynaptic boutons of *Abcd1*$^{-}$ mouse spinal cord neurons

Synaptic mitochondria are crucial to maintain neuronal communication, and their alteration may highly compromise neuronal functions as a whole. [44] Synaptic activity is an energetically expensive process that consumes a large proportion of mitochondrial

ATP production in neurons. In addition to their role as ATP providers, mitochondria are actively recruited to presynapses to control local Ca^{2+} concentrations ($[Ca^{2+}]$) and neurotransmitter release. [44] Synapses are vulnerable to accumulative damage, and defects in synaptic mitochondria will very likely alter synaptic function and be related to a variety of nervous system diseases. [44,45]

To precisely characterize mitochondrial number and morphology in presynaptic boutons, we performed 3D reconstructions from electron microscopy sections of 14-month-old mouse spinal cords in the corticospinal tracts (Fig. 2A). Interestingly, presynaptic boutons of *Wt* mice showed mostly tubular mitochondria, while presynaptic boutons of *Abcd1*$^{-}$ mice contained twice as many rounded mitochondria or so called "donut-shaped" (Fig. 2B and C). Donut-shaped mitochondria constitute an early and reversible hallmark of mitochondrial stress, inducible by respiratory chain poisons or oxidative stress. [33,46,47] These observations suggest that the absence of the peroxisomal ABCD1 transporter affects mitochondrial dynamic imbalance in neuronal axon tracks and presynaptic boutons of spinal cord motor neurons.

Mitochondrial fragmentation is VLCFA and redox-dependent in X-ALD patient fibroblasts

We next used patient-derived fibroblasts as an alternative cellular system to investigate whether excess VLCFAs would generate the observed abnormally shaped mitochondria. X-ALD patient fibroblasts fairly recapitulate the main disease hallmarks, such as (i) VLCFA accumulation, [48] (ii) higher mitochondrial ROS generation and dissipation of mitochondrial membrane potential, [17,24,49] (iii) loss of energetic homeostasis, [20] (iv) altered proteolysis [22,26] and (v) ER stress induction, [50] providing an appropriate *in vitro* model to study the intracellular consequences of peroxisomal ABCD1 transporter loss.
Mitochondrial network morphology between X-ALD patient and nondiseased control fibroblasts presented no detectable differences at baseline, with most mitochondria showing a tubular appearance (Fig. 3A). However, exposure for 24 h to an excess of VLCFA C26:0 induced a reduction in elongated mitochondria (Fig. 3A and B) and increased mitochondrial circularity (Fig. 3A and C) in X-ALD patient fibroblasts, reflecting reduced mitochondrial interconnectivity and increased fragmentation and number of spherical-shaped mitochondria (Fig. 3A and D). In contrast, control fibroblasts

showed no alterations in mitochondrial network morphology when exposed to an excess of C26:0 for 24 h (Fig. 3A-D).

Because excess C26:0 produces ROS predominantly of mitochondrial origin, [24,51] we set out to investigate whether antioxidant treatment with N-acetyl-cysteine (NAC) could modify the detected mitochondrial fragmentation. Indeed, coincubation of NAC with C26:0 prevented mitochondrial fragmentation and the formation of donut-shaped swollen globule mitochondria (Fig. 3A-D), indicating that redox imbalance mediates VLCFA-induced mitochondrial fission in this model. Donut- and swollen-globule-shaped mitochondria have been shown to generate medium and high levels of mitochondrial ROS, respectively, [33] suggesting that these observed abnormally shaped mitochondria may constitute the populations that generate the highest levels of ROS both *in vivo* and *in vitro* in the X-ALD models.

Profission DRP1^{S616} is increased in the spinal cord motor neurons of *Abcd1*$^{-}$ mice in an oxidative stress-dependent manner

We hypothesized that the decreased size of mitochondria in the spinal axon tracks of the *Abcd1*$^{-}$ mouse model and patient fibroblasts may reflect an imbalance in mitochondrial dynamics. During fission, cytosolic DRP1 is recruited to the mitochondrial outer membrane, followed by self-oligomerization, into a ring-like structure to sever the mitochondrial membrane by GTP hydrolysis. DRP1 recruitment to the mitochondria is tightly regulated by several posttranslational modifications. Phosphorylation at serine 616 (DRP1^{S616}) induces DRP1 GTPase activity and provokes mitochondrial fragmentation, [52-54] while phosphorylation of DRP1 at serine 637 (DRP1^{S637}) inhibits its GTPase activity. [55-57] Mitochondrial fusion, instead, is an ATP-dependent multistep process that involves the fusion of outer and inner mitochondrial membranes to generate extended networks. It is sequentially coordinated by evolutionarily conserved proteins mitofusins 1 and 2 (MFN1 and MFN2) and optic atrophy 1 (OPA1). [58,59]

We thus set out to investigate the levels of the main players in fusion/fission, such as MFN2, MFN1, OPA1 and DRP1. We found that phosphorylated DRP1^{S616} was increased in the spinal cord protein lysates of *Abcd1*$^{-}$ mice at 12-month-of age (Fig. 4A and B), while at 3 months, the levels remained unchanged compared to those in their *Wt*

littermates (Supplementary Fig. 2A), thus correlating with disease progression. In contrast, no changes were found in the levels of phosphorylated DRP1^{S637} at the ages analyzed (Fig.3A-B and Supplementary Fig. 2A). The protein levels of the key fusion proteins MFN2, MFN1, and OPA1 also remained unaltered (Fig. 4A-B and Supplementary Fig. 2A), suggesting that the increased level of phosphorylated DRP1^{S616} may be a main player in the mitochondrial dynamic imbalance toward fission.

Furthermore, we prepared an enriched mitochondrial fraction of *Abcd1*$^{-}$ mouse spinal cords at 12 months of age and detected increased levels of total DRP1 as well as phosphorylated DRP1^{S616} by western blotting (Fig. 4B), indicating that phosphorylation at S616 may be involved in DRP1 translocation to mitochondria and activation of mitochondrial fission.

Next, we observed a selective increase in the phosphorylated DRP1^{S616} form in spinal cord motor neurons but not in glial cells in paraffin-embedded transverse sections of the spinal cord of *Abcd1*$^{-}$ mice (Fig. 4E).

Oxidative damage is a hallmark of X-ALD and is detectable as early as a year before disease onset is observed in the X-ALD mouse model. [17] We have previously shown that treatment with antioxidants (a combination of Trolox (vitamin E derivative), α-lipoic acid and NAC) efficiently reduces ROS production in X-ALD patients' fibroblasts, reverses oxidative damage to proteins and DNA in the spinal cords of *Abcd1*$^{-}$ mice, and halts axonal degeneration and motor disabilities in the X-ALD mouse model. [28] To determine whether the cellular redox state was involved in DRP1^{S616} phosphorylation *in vivo,* we treated presymptomatic 8-month-old *Abcd1*$^{-}$ mice with the above mentioned combination of antioxidants for 4 months until 12 months of age. Antioxidant treatment in *Abcd1*$^{-}$ mice normalized phosphorylated DRP1^{S616} to *Wt* levels and prevented DRP1 translocation to mitochondria, as revealed by immunoblotting (Fig. 4F and G), indicating that oxidative stress regulates DRP1^{S616} phosphorylation and acts as an upstream activator of the mitochondrial fission machinery in X-ALD.

VLCFAs induce mitochondrial fragmentation through DRP1^{S616} phosphorylation in X-ALD fibroblasts

We next investigated the role of DRP1 in mitochondrial fragmentation induced by incubation of patient fibroblasts with VLCFAs. Notably, within 16 hours of VLCFA exposure, we found that phosphorylated DRP1^{S616} translocated to mitochondria in X-ALD fibroblasts in the absence of mitochondrial fission (Fig. 5A and C). Furthermore, 24 hours after X-ALD fibroblasts were exposed to VLCFAs, we found that DRP1^{S616} was associated with donut- and swollen globule-shaped mitochondria and at proximal/distal ends of fragmented mitochondria (Fig. 5B and D), indicating that translocation of phosphorylated DRP1^{S616} to mitochondria precedes mitochondrial fragmentation upon VLCFAs. We verified these observations by computational fluorescence intensity profiling, which illustrated the fluorescence intensity along a straight line (Fig. 5C and D). The fluorescence intensity profiles of phosphorylated DRP1^{S616} and MitoTracker™ enabled a better understanding of DRP1^{S616} distribution on the mitochondrial network (Fig. 5C and D).

Since the excessive mitochondrial fission observed *in vitro* seemed to be orchestrated by DRP1, we hypothesized that inhibiting DRP1 action would prevent mitochondrial fragmentation. We therefore used a selective heptapeptide inhibitor of activated DRP1-mediated fission, called P110, [60] to treat X-ALD fibroblasts under C26:0 exposure. P110 has been shown to specifically inhibit pathological but not physiological mitochondrial fission and fragmentation. The results indicated that P110 significantly reduced the mitochondrial fragmentation caused by C26:0 (Fig. 5E-G).

Altogether, our data illustrate a plausible sequence of events that may occur in X-ALD fibroblasts upon exposure to C26:0: i) excess VLCFA induces mitochondrial ROS, ii) DRP1 is phosphorylated at S616, iii) DRP1^{S616} translocates to mitochondria, iv) mitochondria become fragmented and donut, globular mitochondria appear, and v) more mitochondrial ROS are generate.

Inhibition of DRP1 prevents mitochondrial fragmentation and protects neurons from degeneration in a *Caenorhabditis elegans* model of X-ALD

We next set out to gain evidence for excessive mitochondrial fission as a culprit for axonal degeneration in X-ALD. To visualize axonal damage, we used an established

Caenorhabditis elegans model for X-ALD. Worms deficient in PMP-4 *(pmp-4(ok396)),* the ortholog of the *ABCD1* gene in *C. elegans*, recapitulate the main disease hallmarks observed in human AMN patients and *Abcd1*$^{-}$ animals, such as i) accumulation of VLCFAs, ii) oxidative damage, iii) mitochondrial redox imbalance and iv) axonal degeneration associated with locomotor dysfunction. [61]

We first examined the morphology and distribution of mitochondria in neuronal cell bodies and in the ventral cord using a pan-neuronal *Prgef-1::mito-1::GFP* transgene in wild-type and *pmp-4(ok396)* worms to visualize mitochondria (Fig. 6A). Aligned with our previous observations of morphological abnormalities of mitochondria in axons and patient fibroblasts, worms deficient for PMP-4 showed a significant increase in smaller mitochondria compared to wild-type worms, where mitochondria formed filamentous tubular networks that encircled the soma perimeter of the adult neuronal cell bodies. Remarkably, RNAi-mediated *drp-1* silencing by siRNA recovered the elongated morphology of mitochondria on neuronal cell bodies of PMP-4-deficient animals (Fig. 6A and B).

We next used the *juIs76 [Punc-25::gfp]* strain, which labels GABAergic D-type motor neurons with GFP [62], and crossed it to PMP-4-deficient worms to generate the strain *pmp-4(ok396); juIs76 [Punc-25::gfp].* We have previously used this strain to visualize axons and cell bodies of the ventral cord, detecting axonal abnormalities such as commissural defects and gaps caused by loss of PMP-4 (Fig. 6C). [61] Notably, depleting *drp-1* by siRNA recovered axonal damage in the *pmp-4(ok396); juIs76 [Punc-25::gfp]* strain (Fig. 6C and D), thus establishing a direct link between aberrant DRP1 activation, mitochondrial dynamics imbalance and axonopathy in the worm model of X-ALD.

Circulating cell-free mitochondrial DNA is increased in the cerebrospinal fluid of adrenomyeloneuropathy patients

Malfunctioning mitochondria may lead to the release of mtDNA into extracellular fluids, with increased circulating cell-free mtDNA (ccfmtDNA) in plasma and CSF reported in primary mitochondrial deletion and depletion syndromes. [40,63]

We formerly described decreased mtDNA copy number levels and general depletion of mitochondrial mass in the spinal cords of the Abcd1 null mouse model, [29] together with

an increased oxidation of mtDNA in the brain white matter of AMN patients and fibroblasts exposed to excess C26:0. [24]

In search of a clinically relevant biomarker of mitochondrial damage in X-ALD, we compared ccfmtDNA copy number in the CSF of adult, symptomatic adrenomyeloneuropathy patients (AMN, *n*=15) versus age-matched male controls (*n*=13). In the control group, ccfmtDNA values ranged from 1.35 to 31.3 copies/µL (mean 14.37 copies/mL; SEM 2.65), whereas for AMN patients, the values ranged from 6.5 to 124 copies/mL (mean 41.78 copies/mL; SEM 4.5). Thus, our results indicate that the ccfmtDNA levels were significantly higher in the AMN group (*P*=0.0002) (Fig. 7). These AMN patient values are similar to those found in patients with point mutations in mitochondrial-encoded genes (MT-ATP6, MT-ND3, MT-TA, MT-TL1 and MT-TK) and higher than the levels seen in patients with mutations in nuclear genes involved in energy metabolism (PDHA1, PDHB, and SLC19A3),[40] which suggests that mitochondrial dysfunction is at the core of X-ALD physiopathogenesis.

Discussion

X-ALD is a peroxisomal *and* mitochondrial disease

This work exposes a major impact of peroxisomal transporter loss on mitochondrial dynamics in mouse and *C. elegans* models of X-ALD and in patient fibroblasts and even reveals *bona fide* markers of mitochondrial disease in patient CSF, which is of potential interest in monitoring disease progression and modification in clinical trials. Validation of the observed raised levels of ccfmtDNA in independent cohorts is warranted.

The increased mitochondria network fragmentation appears to be orchestrated by DRP1 in a redox-dependent manner. In agreement with our results, Tsushima et al. recently revealed that mitochondrial ROS generation caused by lipid overload induced mitochondrial fission through posttranslational modifications of OPA1 and DRP1. [64] Indeed, treatment with a combination of mitochondrial antioxidants (Trolox, Lipoic acid and NAC) is shown here to normalize DRP1 activation *in vivo*, while NAC restores the mitochondrial network in patient fibroblasts. Antioxidant treatment was previously reported to prevent axonal degeneration and locomotor impairment in the same X-ALD

mouse model; [28] thus, it is tempting to speculate that, as shown in *pmp4* worms, increased mitochondrial fission plays a pivotal role in axonal degeneration in this disease. Of note, the accumulation of defective mitochondria might be exacerbated by defective autophagy observed in the Abcd1 null mouse model and patient fibroblasts in a downward spiral type of scenario. [22]

DRP1 as a therapeutic target

As occurs in some instances when novel physiopathogenetic mechanisms are uncovered, our findings unveil a novel therapeutic target for X-ALD, the fission regulator DRP1. Phosphorylated DRP1 ($DRP1^{S616}$) levels are significantly increased in brain tissues of Alzheimer's disease, amyloid-β-treated primary hippocampal neurons, S-nitrosocystein-treated primary cortical neurons, Huntington's disease knock-in mouse-derived striatal cells and in the retina of glaucomatous D2 mice. [52,53,65-67] Here, we observed that increasing $DRP1^{S616}$ phosphorylation correlates with mitochondrial fission in the *Abcd1*$^{-}$ mouse spinal cord. Blocking this fission regulator (pharmacologically with the peptide P110 or genetically by siRNA) rescued mitochondrial morphology in patient fibroblasts and the axonal damage observed in the X-ALD worm model. These results align well with the improvement in mitochondrial function and neuroprotection obtained by P110 treatments in mouse models of AD, ALS, PD, MS or HSP. [60,68-72] Although no long-term studies or human testing have been performed to date, P110 is able to cross the blood–brain barrier and shows substantial and rapid biodistribution after single-dose treatment *in vivo* and *in vitro*. [68,70,73,74] Novel small molecule compounds with similar mechanisms of action targeting the allosteric site of DRP1 have recently been reported. [75] Thus, all of the above findings support the pertinence of therapeutic development of agents preventing pathological mitochondrial fission in rare and common neurodegenerative diseases such as X-ALD.

Organellar cross-talk in neurodegeneration

Peroxisomes cooperate with mitochondria in central routes of cell metabolism, such as the fatty acid beta-oxidation pathway, and both have a crucial function in ROS detoxification, [76-78] with peroxisomes regulating mitochondrial structure and metabolic

functions. For instance, the loss of PEX genes has been shown to alter the structure and number of mitochondria, reduce mitochondrial bioenergetics and increase mitochondrial ROS generation. [79-82] Peroxisome and mitochondria share key regulators for their fission, including DRP1, as well as the docking proteins MFF and FIS1. [83 84] Indeed, patients with mutations in DRP1 and MFF have been identified, [85,86] and show defects in both peroxisomal and mitochondrial dynamics, exhibiting neurological phenotypes. Although several studies have shown that peroxisomes can localize to mitochondria-associated ER membranes (MAMs) and mitochondrial constriction and scission sites, [87-89] the precise mechanisms involved in DRP1-mediated mitochondrial fission in peroxisome-deficient cells remain unknown. We posit that mitochondrial fragmentation may be caused by an excess of unmetabolized VLCFAs forming part of complex lipids at cellular membranes or as bioactive signaling molecules.

Impairment of mitochondrial dynamics in neurodegeneration

Furthermore, we found accumulation of donut-shaped mitochondria in presynaptic boutons in the *Abcd1*$^{-}$ mouse spinal cord, which may contribute to the previously observed axonal damage in this tissue. [90] Synaptic activity is an energetically expensive process that consumes a large proportion of mitochondrial ATP production in neurons. Donut-shaped mitochondria are an early and reversible hallmark of mitochondrial stress, shown to be inducible by respiratory chain poisons; [33,46,47] here, we provide evidence for excess VLCFAs involving oxidative stress as culprits in the generation of aberrant mitochondrial shapes and the ensuing fission. Interestingly, studies in rhesus monkeys revealed that presynaptic boutons harboring donut-shaped mitochondria form abnormal small synaptic contacts, have fewer readily releasable synaptic vesicles and are inversely correlated with working memory performance. [91] The authors also showed that antioxidant treatment reversed donut-mitochondria formation in presynaptic boutons and mitigated cognitive decline. In a similar manner, we posit that the use of a combination of antioxidants in the X-ALD mouse model and NAC in X-ALD fibroblasts prevents DRP1^{S616} phosphorylation, subsequent mitochondrial fragmentation and the accumulation of aberrantly shaped (donut/swollen globule) organelles. These data shed new light on a plausible mode of action of an antioxidant treatment to prevent axonopathy in *Abcd1*$^{-}$ mice, emphasizing its pertinence to the treatment of X-ALD. [28,92-94]

Altogether, our results suggest a causative role for increased mitochondrial fission in axonal demise, since the inhibition of DRP1 by siRNA in the *C. elegans* model of X-ALD prevented axonal degeneration.

Acknowledgements

We thank Cristina Aguilera for her excellent technical assistance. Most of the strains were supplied by the *Caenorhabditis* Genetic Center (CGC).

Funding

This study was supported by the Centre for Biomedical Research on Rare Diseases (CIBERER) (ACCI19-759), the Hesperia Foundation and the Secretariat for Universities and Research of the Ministry of Business and Knowledge of the Government of Catalonia (2017SGR1206), and the Association ASL-HSP to AP. This study was also funded by the Instituto de Salud Carlos III and 'Fondo Europeo de Desarrollo Regional (FEDER), Unión Europea, una manera de hacer Europa' (FIS PI20/00759) to AP and 'La Marató de TV3' Foundation (202006-30) to CC and AP. NL and MR are supported by the Center for Biomedical Research on Rare Diseases (CIBERER). We thank the CERCA Program/Generalitat de Catalunya for institutional support. A.C., J.P. and S.G. were fellows of IDIBELL.

Competing Interests

The authors report no competing interests.

Supplementary Material

Supplementary Table legends

Supplementary Table 1. C.elegans strains

Supplementary Table 2. Primers and probes used for ddPCR

Supplementary Figure legends

Supplementary Figure 1. Mitochondrial fragmentation in small axons from *Abcd1*$^{-}$ mice spinal cord.

(**A**) SEM images from 500 serial sections of 80 nm thick were stacked, aligned, and reconstructed using 3D reconstruction software. Representative 3D reconstructed mitochondria (green) and small axons (≤ 10µm³, beige) of 14 months old WT and *Abcd1*$^{-}$ mice. (**B-D**) Morphometric analysis of (**B**) mitochondrial length, (**C**) volume and (**D**) aspect ratio (1/surface area/volume ratio; 1/(Sa/V) from small axons of WT and *Abcd1*$^{-}$ mice. Mitochondria from small axons (n=50) were taken into analysis for each genotype (n=4). Statistical analysis was done by Wilcoxon rank sum test otherwise (*P<0.05, ***P<0.001), according to the Shapiro-Wilk normality test.

Supplementary Figure 2: Mitochondrial dynamics at 3 months in X-ALD mouse model

(**A**) Representative immunoblots against phosphor-DRP1^{S637}, phosphor-DRP1^{S616}, DRP1, MFN1, MFN2 and OPA1 proteins in the spinal cord tissue at 3 months in *Abcd1*$^{-}$ and WT mice. Blots run in parallel using identical samples are shown. (**B**) Histograms show phosphorylated-DRP1 levels normalized to total DRP1 protein levels and the DRP1, MFN1, MFN2 and OPA1 levels normalized relative to γ-Tubulin (γ-Tub) relative to WT values.

References

1. Detmer SA, Chan DC. Functions and dysfunctions of mitochondrial dynamics. *Nat Rev Mol Cell Biol*. Nov 2007;8(11):870-9.
2. Breitzig MT, Alleyn MD, Lockey RF, Kolliputi N. A Mitochondrial Delicacy: Dynamin-Related Protein 1 and Mitochondrial Dynamics. *Am J Physiol Cell Physiol*. Apr 18 2018;
3. Adebayo M, Singh S, Singh AP, Dasgupta S. Mitochondrial fusion and fission: The fine-tune balance for cellular homeostasis. *FASEB J*. Jun 2021;35(6):e21620. doi:10.1096/fj.202100067R

4. Miwa S, Kashyap S, Chini E, von Zglinicki T. Mitochondrial dysfunction in cell senescence and aging. *J Clin Invest*. Jul 1 2022;132(13)doi:10.1172/jci158447
5. Karbowski M, Neutzner A. Neurodegeneration as a consequence of failed mitochondrial maintenance. *Acta Neuropathol*. Feb 2012;123(2):157-71. doi:10.1007/s00401-011-0921-0
6. Flippo KH, Strack S. Mitochondrial dynamics in neuronal injury, development and plasticity. *J Cell Sci*. Feb 15 2017;130(4):671-681.
7. Pekkurnaz G, Wang X. Mitochondrial heterogeneity and homeostasis through the lens of a neuron. *Nat Metab*. Jul 2022;4(7):802-812. doi:10.1038/s42255-022-00594-w
8. Turk BR, Theda C, Fatemi A, Moser AB. X-linked adrenoleukodystrophy: Pathology, pathophysiology, diagnostic testing, newborn screening and therapies. *Int J Dev Neurosci*. Feb 2020;80(1):52-72. doi:10.1002/jdn.10003
9. Moser AB, Fatemi A. Newborn Screening and Emerging Therapies for X-Linked Adrenoleukodystrophy. *JAMA Neurol*. Oct 1 2018;75(10):1175-1176. doi:10.1001/jamaneurol.2018.1585
10. Powers JM, DeCiero DP, Ito M, Moser AB, Moser HW. Adrenomyeloneuropathy: a neuropathologic review featuring its noninflammatory myelopathy. *J Neuropathol Exp Neurol*. Feb 2000;59(2):89-102.
11. Moser H, Smith, KD, Watkins, PA, Powers, J, Moser, AB. X-linked adrenoleukodystrophy. In: Scriver C, ed. *The Metabolic and Molecular Bases of Inherited disease*. 8th ed. McGraw-Hill; 2001:3257-3301.
12. Ferrer I, Aubourg P, Pujol A. General aspects and neuropathology of X-linked adrenoleukodystrophy. *Brain Pathol*. Jul 2010;20(4):817-30. doi:10.1111/j.1750-3639.2010.00390.x
13. Moser HW, Moser AB, Kawamura N*, et al*. Adrenoleukodystrophy: elevated C26 fatty acid in cultured skin fibroblasts. *Ann Neurol*. Jun 1980;7(6):542-9. doi:10.1002/ana.410070607
14. Kemp S, Huffnagel IC, Linthorst GE, Wanders RJ, Engelen M. Adrenoleukodystrophy - neuroendocrine pathogenesis and redefinition of natural history. *Nat Rev Endocrinol*. Oct 2016;12(10):606-15. doi:10.1038/nrendo.2016.90
15. Pujol A, Hindelang C, Callizot N, Bartsch U, Schachner M, Mandel JL. Late onset neurological phenotype of the X-ALD gene inactivation in mice: a mouse model for adrenomyeloneuropathy. *Hum Mol Genet*. Mar 1 2002;11(5):499-505. doi:10.1093/hmg/11.5.499
16. Pujol A, Ferrer I, Camps C*, et al*. Functional overlap between ABCD1 (ALD) and ABCD2 (ALDR) transporters: a therapeutic target for X-adrenoleukodystrophy. *HumMolGenet*. 12/1/2004 2004;13(23):2997-3006. doi:10.1093/hmg/ddh323
17. Fourcade S, Lopez-Erauskin J, Galino J*, et al*. Early oxidative damage underlying neurodegeneration in X-adrenoleukodystrophy. *Hum Mol Genet*. Jun 15 2008;17(12):1762-73. doi:10.1093/hmg/ddn085
18. Lopez-Erauskin J, Ferrer I, Galea E, Pujol A. Cyclophilin D as a potential target for antioxidants in neurodegeneration: the X-ALD case. *Biol Chem*. May 2013;394(5):621-9. doi:10.1515/hsz-2012-0323
19. Ranea-Robles P, Galino J, Espinosa L*, et al*. Modulation of mitochondrial and inflammatory homeostasis through RIP140 is neuroprotective in an adrenoleukodystrophy mouse model. *Neuropathol Appl Neurobiol*. Feb 2022;48(1):e12747. doi:10.1111/nan.12747

20. Galino J, Ruiz M, Fourcade S, *et al*. Oxidative damage compromises energy metabolism in the axonal degeneration mouse model of X-adrenoleukodystrophy. *Antioxid Redox Signal*. Oct 15 2011;15(8):2095-107. doi:10.1089/ars.2010.3877
21. Fourcade S, Ferrer I, Pujol A. Oxidative stress, mitochondrial and proteostasis malfunction in adrenoleukodystrophy: A paradigm for axonal degeneration. *Free Radic Biol Med*. Nov 2015;88(Pt A):18-29. doi:10.1016/j.freeradbiomed.2015.05.041
22. Launay N, Aguado C, Fourcade S, *et al*. Autophagy induction halts axonal degeneration in a mouse model of X-adrenoleukodystrophy. *Acta Neuropathol*. Mar 2015;129(3):399-415. doi:10.1007/s00401-014-1378-8
23. Schluter A, Espinosa L, Fourcade S, *et al*. Functional genomic analysis unravels a metabolic-inflammatory interplay in adrenoleukodystrophy. *Hum Mol Genet*. Mar 1 2012;21(5):1062-77. doi:10.1093/hmg/ddr536
24. Lopez-Erauskin J, Galino J, Ruiz M, *et al*. Impaired mitochondrial oxidative phosphorylation in the peroxisomal disease X-linked adrenoleukodystrophy. *Hum Mol Genet*. Aug 15 2013;22(16):3296-305. doi:10.1093/hmg/ddt186
25. Lu JF, Lawler AM, Watkins PA, *et al*. A mouse model for X-linked adrenoleukodystrophy. *ProcNatlAcadSciUSA*. 8/19/1997 1997;94(17):9366-9371. doi:10.1073/pnas.94.17.9366
26. Launay N, Ruiz M, Fourcade S, *et al*. Oxidative stress regulates the ubiquitin-proteasome system and immunoproteasome functioning in a mouse model of X-adrenoleukodystrophy. *Brain*. Mar 2013;136(Pt 3):891-904. doi:10.1093/brain/aws370
27. Ferrer I, Kapfhammer JP, Hindelang C, *et al*. Inactivation of the peroxisomal ABCD2 transporter in the mouse leads to late-onset ataxia involving mitochondria, Golgi and endoplasmic reticulum damage. *Hum Mol Genet*. Dec 1 2005;14(23):3565-77. doi:10.1093/hmg/ddi384
28. Lopez-Erauskin J, Fourcade S, Galino J, *et al*. Antioxidants halt axonal degeneration in a mouse model of X-adrenoleukodystrophy. *Ann Neurol*. Jul 2011;70(1):84-92. doi:10.1002/ana.22363
29. Morato L, Galino J, Ruiz M, *et al*. Pioglitazone halts axonal degeneration in a mouse model of X-linked adrenoleukodystrophy. *Brain*. Aug 2013;136(Pt 8):2432-43. doi:10.1093/brain/awt143
30. Loson OC, Song Z, Chen H, Chan DC. Fis1, Mff, MiD49, and MiD51 mediate Drp1 recruitment in mitochondrial fission. *Mol Biol Cell*. Mar 2013;24(5):659-67.
31. Peng JY, Lin CC, Chen YJ, *et al*. Automatic morphological subtyping reveals new roles of caspases in mitochondrial dynamics. *PLoS Comput Biol*. Oct 2011;7(10):e1002212.
32. Rosivatz E, Woscholski R. Removal or masking of phosphatidylinositol(4,5)bisphosphate from the outer mitochondrial membrane causes mitochondrial fragmentation. *Cell Signal*. Feb 2011;23(2):478-86.
33. Ahmad T, Aggarwal K, Pattnaik B, *et al*. Computational classification of mitochondrial shapes reflects stress and redox state. *Cell Death Dis*. Jan 17 2013;4:e461.
34. Dagda RK, Cherra SJ, 3rd, Kulich SM, Tandon A, Park D, Chu CT. Loss of PINK1 function promotes mitophagy through effects on oxidative stress and mitochondrial fission. *J Biol Chem*. May 15 2009;284(20):13843-55.
35. Fiala JC. Reconstruct: a free editor for serial section microscopy. *J Microsc*. Apr 2005;218(Pt 1):52-61.
36. Kamath RS, Fraser AG, Dong Y, *et al*. Systematic functional analysis of the Caenorhabditis elegans genome using RNAi. *Nature*. Jan 16 2003;421(6920):231-7.

37. Toth ML, Melentijevic I, Shah L*, et al*. Neurite sprouting and synapse deterioration in the aging Caenorhabditis elegans nervous system. *J Neurosci*. Jun 27 2012;32(26):8778-90.
38. Earls LR, Hacker ML, Watson JD, Miller DM, 3rd. Coenzyme Q protects Caenorhabditis elegans GABA neurons from calcium-dependent degeneration. *Proc Natl Acad Sci U S A*. Aug 10 2010;107(32):14460-5.
39. Coppa A, Guha S, Parameswaran J*, et al*. A C.elegans model of X-adrenoleukodystrophy by inactivating the homolog of the Abcd1 transporter, the pmp-4 gene in prep;
40. Trifunov S, Paredes-Fuentes AJ, Badosa C*, et al*. Circulating Cell-Free Mitochondrial DNA in Cerebrospinal Fluid as a Biomarker for Mitochondrial Diseases. *Clin Chem*. Aug 5 2021;67(8):1113-1121. doi:10.1093/clinchem/hvab091
41. Podlesniy P, Trullas R. Biomarkers in Cerebrospinal Fluid: Analysis of Cell-Free Circulating Mitochondrial DNA by Digital PCR. *Methods Mol Biol*. 2018;1768:111-126. doi:10.1007/978-1-4939-7778-9_7
42. Trifunov S, Pyle A, Valentino ML*, et al*. Clonal expansion of mtDNA deletions: different disease models assessed by digital droplet PCR in single muscle cells. *Sci Rep*. Aug 3 2018;8(1):11682. doi:10.1038/s41598-018-30143-z
43. Engelen M, Kemp S, Poll-The BT. X-linked adrenoleukodystrophy: pathogenesis and treatment. *Curr Neurol Neurosci Rep*. Oct 2014;14(10):486.
44. Devine MJ, Kittler JT. Mitochondria at the neuronal presynapse in health and disease. *Nat Rev Neurosci*. Jan 19 2018;19(2):63-80.
45. Morton H, Kshirsagar S, Orlov E*, et al*. Defective mitophagy and synaptic degeneration in Alzheimer's disease: Focus on aging, mitochondria and synapse. *Free Radic Biol Med*. Aug 20 2021;172:652-667. doi:10.1016/j.freeradbiomed.2021.07.013
46. Liu X, Hajnoczky G. Altered fusion dynamics underlie unique morphological changes in mitochondria during hypoxia-reoxygenation stress. *Cell Death Differ*. Oct 2011;18(10):1561-72.
47. Fourcade S, Lopez-Erauskin J, Ruiz M, Ferrer I, Pujol A. Mitochondrial dysfunction and oxidative damage cooperatively fuel axonal degeneration in X-linked adrenoleukodystrophy. *Biochimie*. Mar 2014;98:143-9. doi:10.1016/j.biochi.2013.09.012
48. Wanders RJ, van Roermund CW, van Wijland MJ*, et al*. X-linked adrenoleukodystrophy: identification of the primary defect at the level of a deficient peroxisomal very long chain fatty acyl-CoA synthetase using a newly developed method for the isolation of peroxisomes from skin fibroblasts. *J Inherit Metab Dis*. 1988;11 Suppl 2:173-7.
49. Lopez-Erauskin J, Galino J, Bianchi P*, et al*. Oxidative stress modulates mitochondrial failure and cyclophilin D function in X-linked adrenoleukodystrophy. *Brain*. Dec 2012;135(Pt 12):3584-98. doi:10.1093/brain/aws292
50. Launay N, Ruiz M, Grau L*, et al*. Tauroursodeoxycholic bile acid arrests axonal degeneration by inhibiting the unfolded protein response in X-linked adrenoleukodystrophy. *Acta Neuropathol*. Feb 2017;133(2):283-301. doi:10.1007/s00401-016-1655-9
51. Kruska N, Schonfeld P, Pujol A, Reiser G. Astrocytes and mitochondria from adrenoleukodystrophy protein (ABCD1)-deficient mice reveal that the adrenoleukodystrophy-associated very long-chain fatty acids target several cellular energy-dependent functions. *Biochim Biophys Acta*. May 2015;1852(5):925-36. doi:10.1016/j.bbadis.2015.01.005

52. Roe AJ, Qi X. Drp1 phosphorylation by MAPK1 causes mitochondrial dysfunction in cell culture model of Huntington's disease. *Biochem Biophys Res Commun*. Feb 5 2018;496(2):706-711. doi:10.1016/j.bbrc.2018.01.114
53. Lee DS, Kim JE. PDI-mediated S-nitrosylation of DRP1 facilitates DRP1-S616 phosphorylation and mitochondrial fission in CA1 neurons. *Cell Death Dis*. Aug 29 2018;9(9):869. doi:10.1038/s41419-018-0910-5
54. Cho B, Choi SY, Cho HM, Kim HJ, Sun W. Physiological and pathological significance of dynamin-related protein 1 (drp1)-dependent mitochondrial fission in the nervous system. *Exp Neurobiol*. Sep 2013;22(3):149-57. doi:10.5607/en.2013.22.3.149
55. Yu R, Liu T, Ning C*, et al*. The phosphorylation status of Ser-637 in dynamin-related protein 1 (Drp1) does not determine Drp1 recruitment to mitochondria. *J Biol Chem*. Nov 15 2019;294(46):17262-17277. doi:10.1074/jbc.RA119.008202
56. Chang CR, Blackstone C. Dynamic regulation of mitochondrial fission through modification of the dynamin-related protein Drp1. *Ann N Y Acad Sci*. Jul 2010;1201:34-9.
57. Cribbs JT, Strack S. Reversible phosphorylation of Drp1 by cyclic AMP-dependent protein kinase and calcineurin regulates mitochondrial fission and cell death. *EMBO reports*. Oct 2007;8(10):939-44.
58. Ranieri M, Brajkovic S, Riboldi G*, et al*. Mitochondrial fusion proteins and human diseases. *Neurol Res Int*. 2013;2013:293893. doi:10.1155/2013/293893
59. Chandhok G, Lazarou M, Neumann B. Structure, function, and regulation of mitofusin-2 in health and disease. *Biol Rev Camb Philos Soc*. May 2018;93(2):933-949. doi:10.1111/brv.12378
60. Qi X, Qvit N, Su YC, Mochly-Rosen D. A novel Drp1 inhibitor diminishes aberrant mitochondrial fission and neurotoxicity. *J Cell Sci*. Feb 1 2013;126(Pt 3):789-802. doi:10.1242/jcs.114439
61. Coppa A, Guha S, Fourcade S*, et al*. The peroxisomal fatty acid transporter ABCD1/PMP-4 is required in the C. elegans hypodermis for axonal maintenance: A worm model for adrenoleukodystrophy. *Free Radic Biol Med*. May 20 2020;152:797-809. doi:10.1016/j.freeradbiomed.2020.01.177
62. Cinar H, Keles S, Jin Y. Expression profiling of GABAergic motor neurons in Caenorhabditis elegans. *Curr Biol*. Feb 22 2005;15(4):340-6.
63. Maresca A, Del Dotto V, Romagnoli M*, et al*. Expanding and validating the biomarkers for mitochondrial diseases. *J Mol Med (Berl)*. Oct 2020;98(10):1467-1478. doi:10.1007/s00109-020-01967-y
64. Tsushima K, Bugger H, Wende AR*, et al*. Mitochondrial Reactive Oxygen Species in Lipotoxic Hearts Induces Post-Translational Modifications of AKAP121, DRP1 and OPA1 That Promote Mitochondrial Fission. *Circ Res*. Nov 1 2017;
65. Yan J, Liu XH, Han MZ*, et al*. Blockage of GSK3beta-mediated Drp1 phosphorylation provides neuroprotection in neuronal and mouse models of Alzheimer's disease. *Neurobiol Aging*. Jan 2015;36(1):211-27. doi:10.1016/j.neurobiolaging.2014.08.005
66. Cho DH, Nakamura T, Fang J*, et al*. S-nitrosylation of Drp1 mediates beta-amyloid-related mitochondrial fission and neuronal injury. *Science*. Apr 03 2009;324(5923):102-5. doi:10.1126/science.1171091
67. Kim KY, Perkins GA, Shim MS*, et al*. DRP1 inhibition rescues retinal ganglion cells and their axons by preserving mitochondrial integrity in a mouse model of glaucoma. *Cell Death Dis*. Aug 6 2015;6:e1839.
68. Joshi AU, Saw NL, Shamloo M, Mochly-Rosen D. Drp1/Fis1 interaction mediates mitochondrial dysfunction, bioenergetic failure and cognitive decline in

Alzheimer's disease. *Oncotarget*. Jan 19 2018;9(5):6128-6143. doi:10.18632/oncotarget.23640
69. Joshi AU, Saw NL, Vogel H, Cunnigham AD, Shamloo M, Mochly-Rosen D. Inhibition of Drp1/Fis1 interaction slows progression of amyotrophic lateral sclerosis. *EMBO Mol Med*. Mar 2018;10(3)doi:10.15252/emmm.201708166
70. Luo F, Herrup K, Qi X, Yang Y. Inhibition of Drp1 hyper-activation is protective in animal models of experimental multiple sclerosis. *Exp Neurol*. Jun 2017;292:21-34.
71. Chen Z, Chai E, Mou Y, Roda RH, Blackstone C, Li XJ. Inhibiting mitochondrial fission rescues degeneration in hereditary spastic paraplegia neurons. *Brain*. Nov 21 2022;145(11):4016-4031. doi:10.1093/brain/awab488
72. Filichia E, Hoffer B, Qi X, Luo Y. Inhibition of Drp1 mitochondrial translocation provides neural protection in dopaminergic system in a Parkinson's disease model induced by MPTP. *Sci Rep*. Sep 13 2016;6:32656. doi:10.1038/srep32656
73. Zhao Y, Sun X, Qi X. Inhibition of Drp1 hyperactivation reduces neuropathology and behavioral deficits in zQ175 knock-in mouse model of Huntington's disease. *Biochem Biophys Res Commun*. Dec 9 2018;507(1-4):319-323. doi:10.1016/j.bbrc.2018.11.031
74. Johnson J, Mercado-Ayón E, Clark E, Lynch D, Lin H. Drp1-dependent peptide reverse mitochondrial fragmentation, a homeostatic response in Friedreich ataxia. *Pharmacol Res Perspect*. May 2021;9(3):e00755. doi:10.1002/prp2.755
75. Rios L, Pokhrel S, Li SJ, Heo G, Haileselassie B, Mochly-Rosen D. Targeting an allosteric site in dynamin-related protein 1 to inhibit Fis1-mediated mitochondrial dysfunction. *Nature communications*. Jul 19 2023;14(1):4356. doi:10.1038/s41467-023-40043-0
76. Wanders RJA, Baes M, Ribeiro D, Ferdinandusse S, Waterham HR. The physiological functions of human peroxisomes. *Physiol Rev*. Jan 1 2023;103(1):957-1024. doi:10.1152/physrev.00051.2021
77. Lodhi IJ, Semenkovich CF. Peroxisomes: a nexus for lipid metabolism and cellular signaling. *Cell Metab*. Mar 4 2014;19(3):380-92.
78. Fransen M, Lismont C, Walton P. The Peroxisome-Mitochondria Connection: How and Why? *Int J Mol Sci*. May 24 2017;18(6)doi:10.3390/ijms18061126
79. Peeters A, Shinde AB, Dirkx R*, et al*. Mitochondria in peroxisome-deficient hepatocytes exhibit impaired respiration, depleted DNA, and PGC-1alpha independent proliferation. *Biochim Biophys Acta*. Feb 2015;1853(2):285-98.
80. Rahim RS, Chen M, Nourse CC, Meedeniya AC, Crane DI. Mitochondrial changes and oxidative stress in a mouse model of Zellweger syndrome neuropathogenesis. *Neuroscience*. Oct 15 2016;334:201-213. doi:10.1016/j.neuroscience.2016.08.001
81. Bülow MH, Wingen C, Senyilmaz D*, et al*. Unbalanced lipolysis results in lipotoxicity and mitochondrial damage in peroxisome-deficient Pex19 mutants. *Mol Biol Cell*. Feb 15 2018;29(4):396-407. doi:10.1091/mbc.E17-08-0535
82. Jiang C, Okazaki T. Control of mitochondrial dynamics and apoptotic pathways by peroxisomes. *Frontiers in cell and developmental biology*. 2022;10:938177. doi:10.3389/fcell.2022.938177
83. Costello JL, Passmore JB, Islinger M, Schrader M. Multi-localized Proteins: The Peroxisome-Mitochondria Connection. *Subcell Biochem*. 2018;89:383-415. doi:10.1007/978-981-13-2233-4_17

84. Tanaka H, Okazaki T, Aoyama S, *et al*. Peroxisomes control mitochondrial dynamics and the mitochondrion-dependent apoptosis pathway. *J Cell Sci*. May 31 2019;132(11)doi:10.1242/jcs.224766
85. Koch J, Feichtinger RG, Freisinger P, *et al*. Disturbed mitochondrial and peroxisomal dynamics due to loss of MFF causes Leigh-like encephalopathy, optic atrophy and peripheral neuropathy. *J Med Genet*. Apr 2016;53(4):270-8. doi:10.1136/jmedgenet-2015-103500
86. Waterham HR, Koster J, van Roermund CW, Mooyer PA, Wanders RJ, Leonard JV. A lethal defect of mitochondrial and peroxisomal fission. *N Engl J Med*. Apr 26 2007;356(17):1736-41.
87. Cohen Y, Klug YA, Dimitrov L, *et al*. Peroxisomes are juxtaposed to strategic sites on mitochondria. *Mol Biosyst*. Jul 2014;10(7):1742-8. doi:10.1039/c4mb00001c
88. Bittner E, Stehlik T, Freitag J. Sharing the wealth: The versatility of proteins targeted to peroxisomes and other organelles. *Frontiers in cell and developmental biology*. 2022;10:934331. doi:10.3389/fcell.2022.934331
89. Shai N, Yifrach E, van Roermund CWT, *et al*. Systematic mapping of contact sites reveals tethers and a function for the peroxisome-mitochondria contact. *Nature communications*. May 2 2018;9(1):1761. doi:10.1038/s41467-018-03957-8
90. Gong Y, Sasidharan N, Laheji F, *et al*. Microglial dysfunction as a key pathological change in adrenomyeloneuropathy. *Ann Neurol*. Nov 2017;82(5):813-827. doi:10.1002/ana.25085
91. Hara Y, Yuk F, Puri R, Janssen WG, Rapp PR, Morrison JH. Presynaptic mitochondrial morphology in monkey prefrontal cortex correlates with working memory and is improved with estrogen treatment. *Proc Natl Acad Sci U S A*. Jan 7 2014;111(1):486-91.
92. Turk BR, Nemeth CL, Marx JS, *et al*. Dendrimer N-acetylcysteine modulates monophagocytic response in adrenoleukodystrophy. *Ann Neurol*. Aug 1 2018;84(3):452-462.
93. Marchetti DP, Steffens L, Jacques CE, *et al*. Oxidative Imbalance, Nitrative Stress, and Inflammation in C6 Glial Cells Exposed to Hexacosanoic Acid: Protective Effect of N-acetyl-L-cysteine, Trolox, and Rosuvastatin. *Cell Mol Neurobiol*. Nov 2018;38(8):1505-1516. doi:10.1007/s10571-018-0626-1
94. Zhou J, Terluk MR, Orchard PJ, Cloyd JC, Kartha RV. N-Acetylcysteine Reverses the Mitochondrial Dysfunction Induced by Very Long-Chain Fatty Acids in Murine Oligodendrocyte Model of Adrenoleukodystrophy. *Biomedicines*. Dec 3 2021;9(12)doi:10.3390/biomedicines9121826

Figure Legends

Figure 1. Mitochondrial fragmentation in axons from the *Abcd1*$^{-}$ mouse spinal cord. (**A**) Representative electron microscopy micrographs from serial block-face scanning electron microscopy (SBF-SEM) of axonal mitochondria in the motor cortico-spinal tract of wild-type (*Wt*) and *Abcd1*$^{-}$ mice at 14 months. (**B**) SEM images from 500 serial Sections 80 nm thick were stacked, aligned, and reconstructed using 3D reconstruction software. Representative 3D reconstructed mitochondria (green) and large axons (≥ 40 µm³, beige) of 14-month-old *Wt* and *Abcd1*$^{-}$ mice. (**C-E**) Morphometric analysis of (**C**)

mitochondrial length, (**D**) volume and (**E**) aspect ratio (1/surface area/volume ratio; 1/(Sa/V)) from large axons of WT and *Abcd1*$^{-}$ mice. Mitochondria from large axons (n=25) were analyzed for each genotype (n=4; *P<0.05, ***P<0.001, Wilcoxon rank sum test otherwise according to the Shapiro–Wilk normality test).

Figure 2. Accumulation of donut-shaped mitochondria in synaptic boutons from the *Abcd1*$^{-}$ mouse spinal cord.

(**A, a-e**) Representative serial electron micrographs of boutons containing donut-shaped mitochondria from the *Abcd1*$^{-}$ mouse spinal cord at 14 months (14 m) of age. Dotted red lines outline mitochondria, the blue area delimitates the axonal bouton, and black arrowheads point to the active zone. (**B**) 3D reconstruction of 40 axonal bouton areas (beige) and residing mitochondria with tubular (green), small globule (blue) or donut-shaped (red) morphologies using serial block-face scanning electron microscopy (SBF-SEM) section micrographs. **(C)** Quantification of synaptic boutons displaying tubular (green), small globules (blue) or donut-shaped (red) mitochondria in wild-type (*Wt*) and *Abcd1*$^{-}$ mouse spinal cords at 14 months.

Figure 3. VLCFAs induce redox-dependent mitochondrial fragmentation and donut-shaped mitochondria formation in X-ALD fibroblasts.

(**A**) MitoTracker™ (MitoT) staining of control (CTL) and X-ALD human fibroblasts (X-ALD) exposed to VLCFA (C26:0; 50 µM, 24 h) in the presence or absence of *N*-acetyl cysteine (NAC, 1 mM, 24 h). Scale bar= 20 µm. A zoomed-in view is shown for each image with a scale bar of 5 µm. Individual mitochondria are color-coded as follows: green-long linear tubules, light blue-short linear tubules, dark blue-fragmented, small globules, red-donuts and cyan-swollen globules. **(B-D)** Quantification of (**B**) mitochondrial length, (**C**) mitochondrial circularity and (**D**) percentage of mitochondrial subtype based on morphology under the different conditions analyzed. n > 20 cells for each genotype and condition. X-ALD (n=5) and control (CTL, n=5) fibroblasts. All data are shown as the mean ± SD. Results were obtained from 2 independent experiments. *P < 0.05, ***P < 0.001. All data analysis were performed using 1-way ANOVA followed by Tukey's test for multiple comparisons.

Figure 4. Oxidative stress regulates DRP1 phosphorylation and subcellular localization in the *Abcd1*$^{-}$ mouse spinal cord.

(**A**) Representative immunoblots against phosphor-DRP1^{S616}, phosphor-DRP1^{S637}, DRP1, MFN1, MFN2 and OPA1 proteins in the spinal cord tissue at 12 months (12 m) in *Abcd1*$^{-}$ and *Wt* mice. Blots run in parallel using identical samples are shown. (**B**) Quantification of phosphorylated-DRP1/total DRP1 ratios and the DRP1, MFN1, MFN2 and OPA1 levels normalized relative to γ-Tubulin (γ-Tub) relative to *Wt* values. (**C**) Immunoblots of phosphorylated DRP1^{S616}, DRP1^{S637} and total DRP1 in the enriched mitochondrial fraction from the spinal cords of 12-month-old *Wt* and *Abcd1*$^{-}$ mice. Blots run in parallel using identical samples are shown. (**D**) Quantification of the phosphorylated DRP1^{S616}/total DRP1 ratio and the DRP1 level in *Abcd1*$^{-}$ mice relative to *Wt* values. (**E**) Immunofluorescence of phosphorylated DRP1^{S616} with neurons (NeuN) in the ventral horn of spinal cord sections from 12-month-old *Wt* and *Abcd1*$^{-}$ mice. Nuclei were counterstained with DAPI. Scale bar = 25 µm. A zoomed-in view is shown for each image with a scale bar of 10 µm. (**F**) Immunoblots showing the levels of the phosphorylated form of DRP1 (DRP1^{S616}) and total DRP1 in the spinal cord of *Wt*, *Abcd1*$^{-}$ mice and antioxidant-treated (*Abcd1*$^{-}$ + Antx) *Abcd1*$^{-}$ mice at 12 months of age. Blots run in parallel using identical samples are shown. (**G**) Quantification of the phosphorylated DRP1^{S616}/total DRP1 ratio and the DRP1 levels in total and mitochondria-enriched extracts from *Abcd1*$^{-}$ mice relative to *Wt* values. All values are expressed as the mean ± SD (n=10 by genotype and condition in **B, D** and **G**; *P<0.05, one-way ANOVA followed by Tukey's HSD post hoc test).

Figure 5. VLCFA induces mitochondrial fragmentation in a DRP1-dependent manner

(**A-B**) Immunofluorescence using phosphorylated DRP1^{S616} antibody (green) and MitoTracker™ (red) in control (CTL) and X-ALD human fibroblasts (X-ALD) exposed to C26:0 for (**A**) 16 h and (**B**) 24 h. (**C-D**) Fluorescence intensity profiles of the mitochondria revealed by MitoTracker™ staining (red) and DRP1^{S616} (green) along a straight line from (**A**) and (**B**) (white line).

(E) MitoTracker™ (MitoT) and DAPI staining of human control (CTL) and X-ALD fibroblasts exposed to VLCFA (C26:0; 50 µM, 24 h) without or with P110 (1 µM, 24 h). Scale bar =25 µm. A zoomed-in view is shown for each image with a scale bar of 5 µm. **(F-G**) Quantification of (**F**) mitochondrial elongation and (**G**) mitochondrial circularity under the different conditions analyzed. Results were obtained from 2 independent

experiments. All values are expressed as the mean ± SD (*n*=5 by genotype and condition in **B** and **C**; **P*<0.05 and ****P*<0.001, one-way ANOVA followed by Tukey's HSD post hoc test).

Figure 6. Inhibition of DRP1 improves mitochondrial morphology and axonal degeneration in an X-ALD worm model.

(**A-D**) Synchronized L1 worms at the indicated genotypes were treated with *RNAi* against *drp-1* or empty vector control (EV). (**A**) (*a*) Schematic representation of neurons in the ventral nerve cord is shown in the upper panel. (*b-e*) Representative fluorescence images of a Pan-neuronal *Prgef-1::mito-1::GFP* transgene in (*b*) wild-type (WT), (*c*) *pmp-4(ok396)* worms, (*d*) wild-type (WT) worms treated with *drp-1* siRNA, and (*e*) *pmp-4(ok396)* worms treated with *drp-1* siRNA. Scale bar =10 μm. (**B**) Quantification of mitochondrial size of neuron cell bodies. (**C**) (*a*) Schematic representation of the *C. elegans* GABAergic nervous system. (*b-e*) Representative images of GABA neuron cell body processes in the ventral nerve cord and dorsally projecting commissures labeled with GFP in (*b*) *juIs76 [Punc-25::gfp]*, (*c*) *pmp-4(ok396); juIs76 [Punc-25::gfp]*, (*d*) *juIs76 [Punc-25::gfp]* treated with *drp-1* RNAi, and (*e*) *pmp-4(ok396); juIs76 [Punc-25::gfp]* treated with *drp-1* RNAi at the L4 stage. Commissural abnormalities and gaps in the dorsal and ventral cord are labeled with white arrows. Scale = 25 μm. (**D**) Quantification of the axonal defects. All values are expressed as the mean ± SD (between 20 and 25 cell bodies were analyzed per genotype and condition in **B**; between 30 and 40 animals were analyzed per genotype and condition in **D**; **P*<0.05 and ****P*<0.001, one-way ANOVA followed by Tukey's HSD post hoc test).

Figure 7. Cell-free circulating mitochondrial DNA (ccfmtDNA) is increased in X-ALD cerebrospinal fluid

Quantification of ccfmtDNA in the CSF of AMN patients (*n*=15) and sex and age-matched controls (*n*=13). Values are expressed as the number of copies per microliter. mean ± SEM. ****P*<0.001, two-tailed Mann–Whitney test.

Figure1

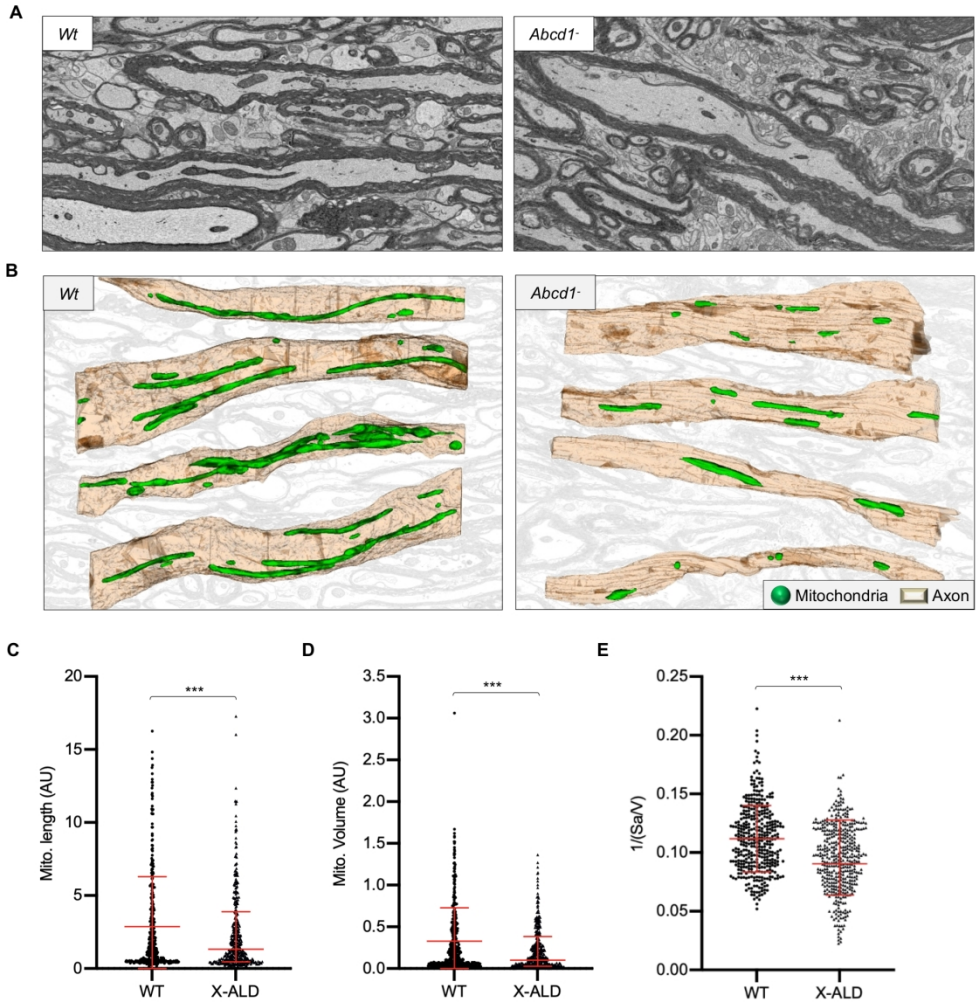

Figure 1. Mitochondrial fragmentation in axons from the Abcd1- mouse spinal cord.
(A) Representative electron microscopy micrographs from serial block-face scanning electron microscopy (SBF-SEM) of axonal mitochondria in the motor cortico-spinal tract of wild-type (Wt) and Abcd1- mice at 14 months. (B) SEM images from 500 serial Sections 80 nm thick were stacked, aligned, and reconstructed using 3D reconstruction software. Representative 3D reconstructed mitochondria (green) and large axons (≥ 40 µm³, beige) of 14-month-old Wt and Abcd1- mice. (C-E) Morphometric analysis of (C) mitochondrial length, (D) volume and (E) aspect ratio (1/surface area/volume ratio; 1/(Sa/V)) from large axons of WT and Abcd1- mice. Mitochondria from large axons (n=25) were analyzed for each genotype (n=4; *P<0.05, ***P<0.001, Wilcoxon rank sum test otherwise according to the Shapiro–Wilk normality test).

174x192mm (300 x 300 DPI)

Figure2

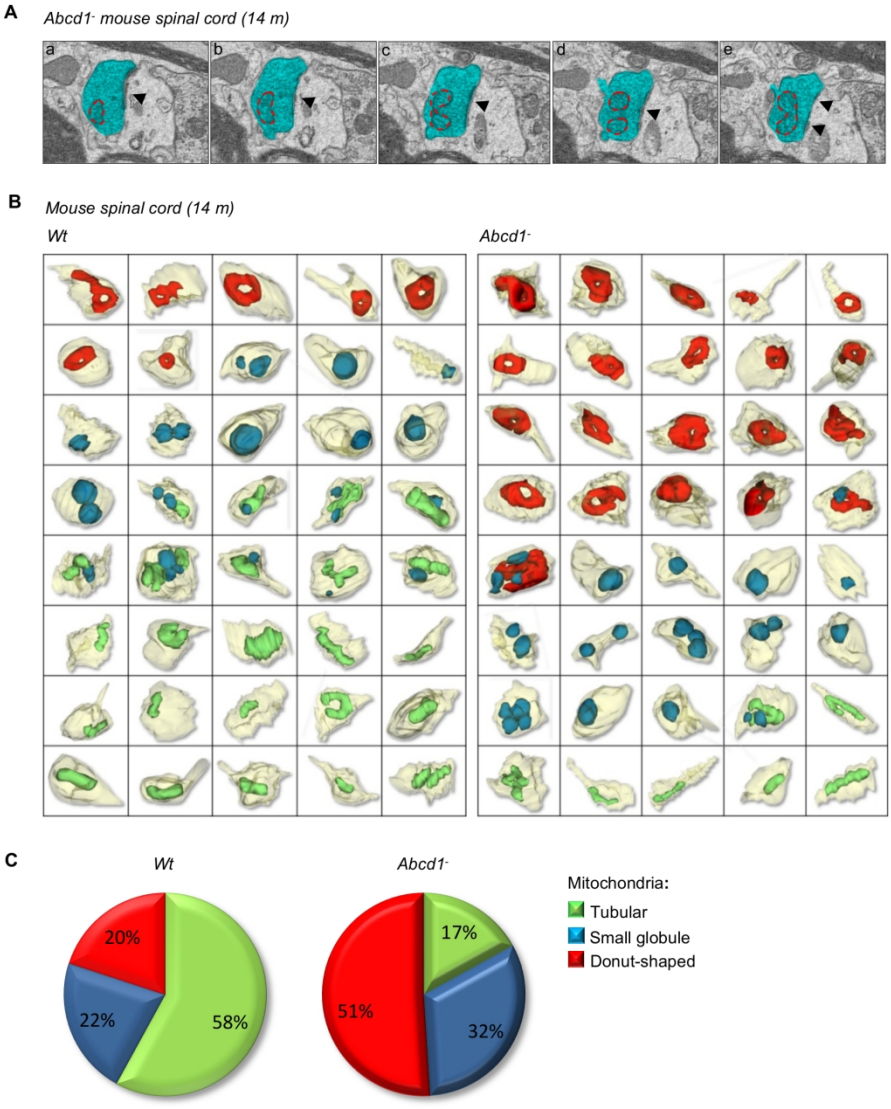

Figure 2. Accumulation of donut-shaped mitochondria in synaptic boutons from the Abcd1- mouse spinal cord.
(A, a-e) Representative serial electron micrographs of boutons containing donut-shaped mitochondria from the Abcd1- mouse spinal cord at 14 months (14 m) of age. Dotted red lines outline mitochondria, the blue area delimitates the axonal bouton, and black arrowheads point to the active zone. (B) 3D reconstruction of 40 axonal bouton areas (beige) and residing mitochondria with tubular (green), small globule (blue) or donut-shaped (red) morphologies using serial block-face scanning electron microscopy (SBF-SEM) section micrographs. (C) Quantification of synaptic boutons displaying tubular (green), small globules (blue) or donut-shaped (red) mitochondria in wild-type (Wt) and Abcd1- mouse spinal cords at 14 months.

155x202mm (300 x 300 DPI)

Figure 3

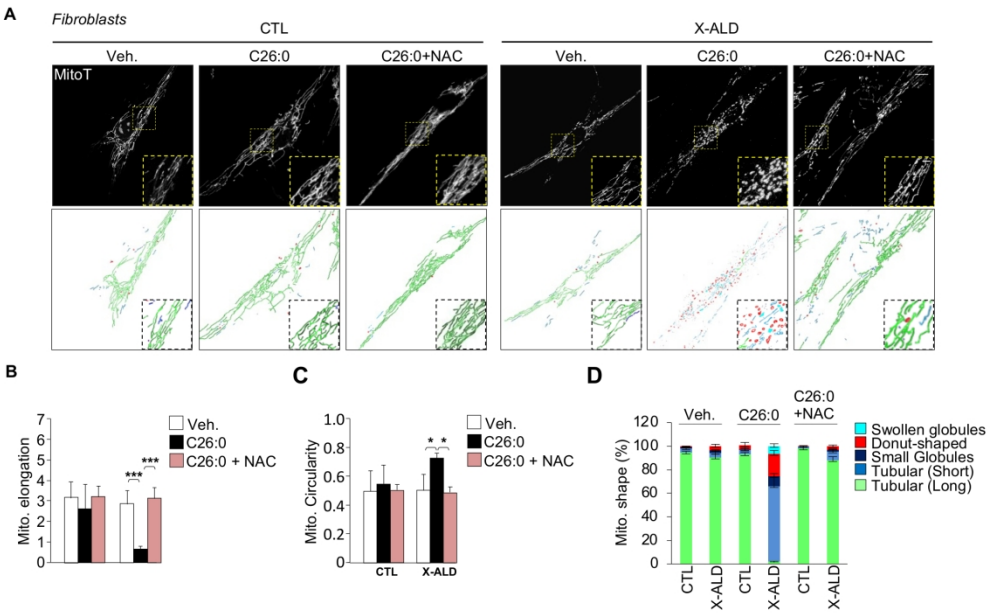

Figure 3. VLCFAs induce redox-dependent mitochondrial fragmentation and donut-shaped mitochondria formation in X-ALD fibroblasts.
(A) MitoTrackerTM (MitoT) staining of control (CTL) and X-ALD human fibroblasts (X-ALD) exposed to VLCFA (C26:0; 50 µM, 24 h) in the presence or absence of N-acetyl cysteine (NAC, 1 mM, 24 h). Scale bar= 20 µm. A zoomed-in view is shown for each image with a scale bar of 5 µm. Individual mitochondria are color-coded as follows: green-long linear tubules, light blue-short linear tubules, dark blue-fragmented, small globules, red-donuts and cyan-swollen globules. (B-D) Quantification of (B) mitochondrial length, (C) mitochondrial circularity and (D) percentage of mitochondrial subtype based on morphology under the different conditions analyzed. n > 20 cells for each genotype and condition. X-ALD (n=5) and control (CTL, n=5) fibroblasts. All data are shown as the mean ± SD. Results were obtained from 2 independent experiments. *P < 0.05, ***P < 0.001. All data analysis were performed using 1-way ANOVA followed by Tukey's test for multiple comparisons.

185x131mm (300 x 300 DPI)

Figure 4

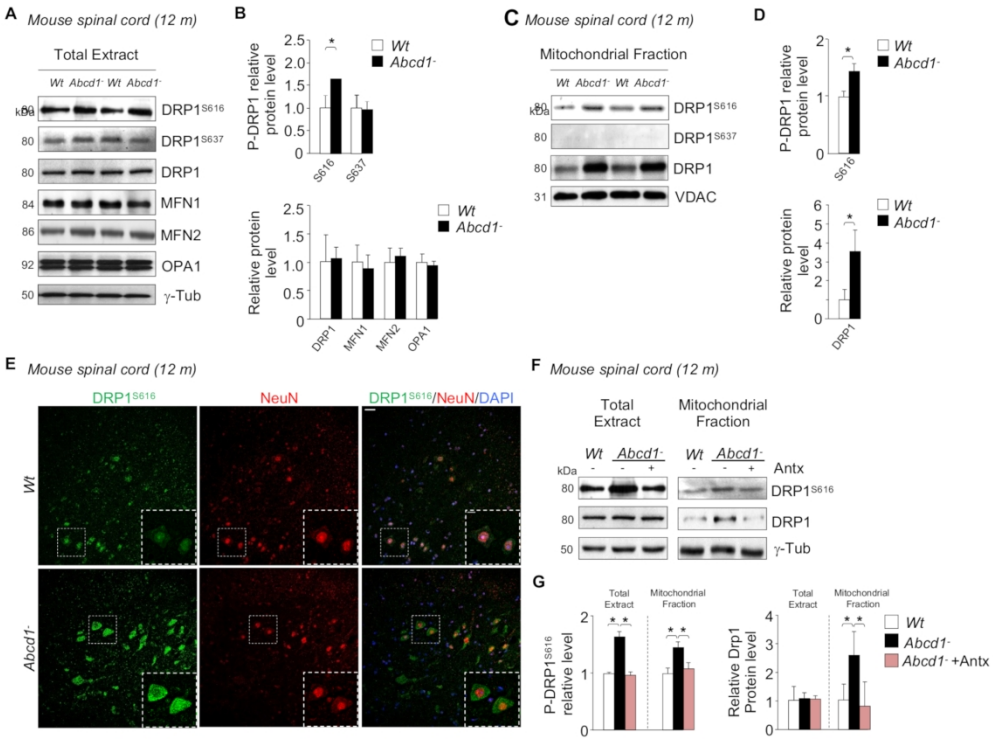

Figure 4. Oxidative stress regulates DRP1 phosphorylation and subcellular localization in the Abcd1- mouse spinal cord.

(A) Representative immunoblots against phosphor-DRP1S616, phosphor-DRP1S637, DRP1, MFN1, MFN2 and OPA1 proteins in the spinal cord tissue at 12 months (12 m) in Abcd1- and Wt mice. Blots run in parallel using identical samples are shown. (B) Quantification of phosphorylated-DRP1/total DRP1 ratios and the DRP1, MFN1, MFN2 and OPA1 levels normalized relative to γ-Tubulin (γ-Tub) relative to Wt values. (C) Immunoblots of phosphorylated DRP1S616, DRP1S637 and total DRP1 in the enriched mitochondrial fraction from the spinal cords of 12-month-old Wt and Abcd1- mice. Blots run in parallel using identical samples are shown. (D) Quantification of the phosphorylated DRP1S616/total DRP1 ratio and the DRP1 level in Abcd1- mice relative to Wt values. (E) Immunofluorescence of phosphorylated DRP1S616 with neurons (NeuN) in the ventral horn of spinal cord sections from 12-month-old Wt and Abcd1- mice. Nuclei were counterstained with DAPI. Scale bar = 25 μm. A zoomed-in view is shown for each image with a scale bar of 10 μm. (F) Immunoblots showing the levels of the phosphorylated form of DRP1 (DRP1S616) and total DRP1 in the spinal cord of Wt, Abcd1- mice and antioxidant-treated (Abcd1- + Antx) Abcd1- mice at 12 months of age. Blots run in parallel using identical samples are shown. (G) Quantification of the phosphorylated DRP1S616/total DRP1 ratio and the DRP1 levels in total and mitochondria-enriched extracts from Abcd1- mice relative to Wt values. All values are expressed as the mean ± SD (n=10 by genotype and condition in B, D and G; *P<0.05, one-way ANOVA followed by Tukey's HSD post hoc test).

185x150mm (300 x 300 DPI)

Figure 5

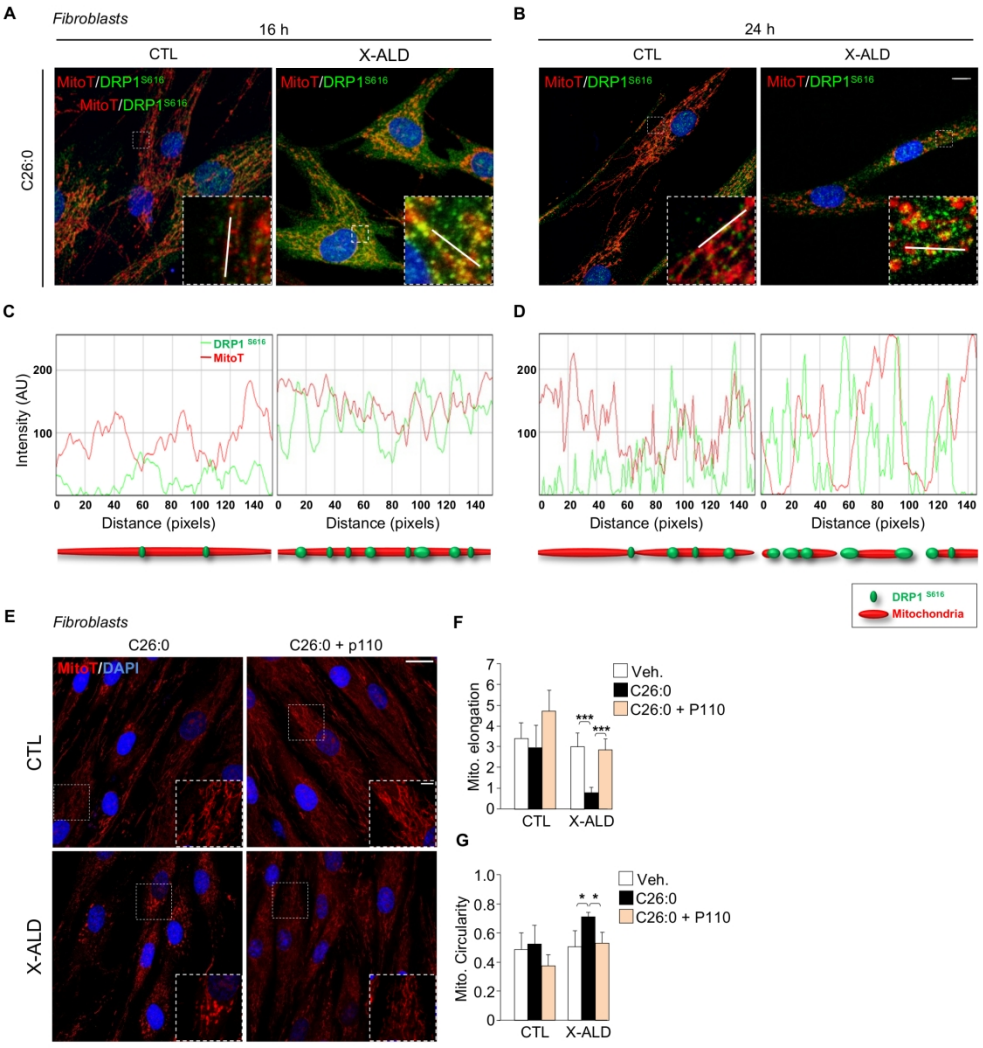

Figure 5. VLCFA induces mitochondrial fragmentation in a DRP1-dependent manner
(A-B) Immunofluorescence using phosphorylated DRP1S616 antibody (green) and MitoTrackerTM (red) in control (CTL) and X-ALD human fibroblasts (X-ALD) exposed to C26:0 for (A) 16 h and (B) 24 h. (C-D) Fluorescence intensity profiles of the mitochondria revealed by MitoTrackerTM staining (red) and DRP1S616 (green) along a straight line from (A) and (B) (white line).
(E) MitoTrackerTM (MitoT) and DAPI staining of human control (CTL) and X-ALD fibroblasts exposed to VLCFA (C26:0; 50 µM, 24 h) without or with P110 (1 µM, 24 h). Scale bar =25 µm. A zoomed-in view is shown for each image with a scale bar of 5 µm. (F-G) Quantification of (F) mitochondrial elongation and (G) mitochondrial circularity under the different conditions analyzed. Results were obtained from 2 independent experiments. All values are expressed as the mean ± SD (n=5 by genotype and condition in B and C; *P<0.05 and ***P<0.001, one-way ANOVA followed by Tukey's HSD post hoc test).

183x209mm (300 x 300 DPI)

Figure 6

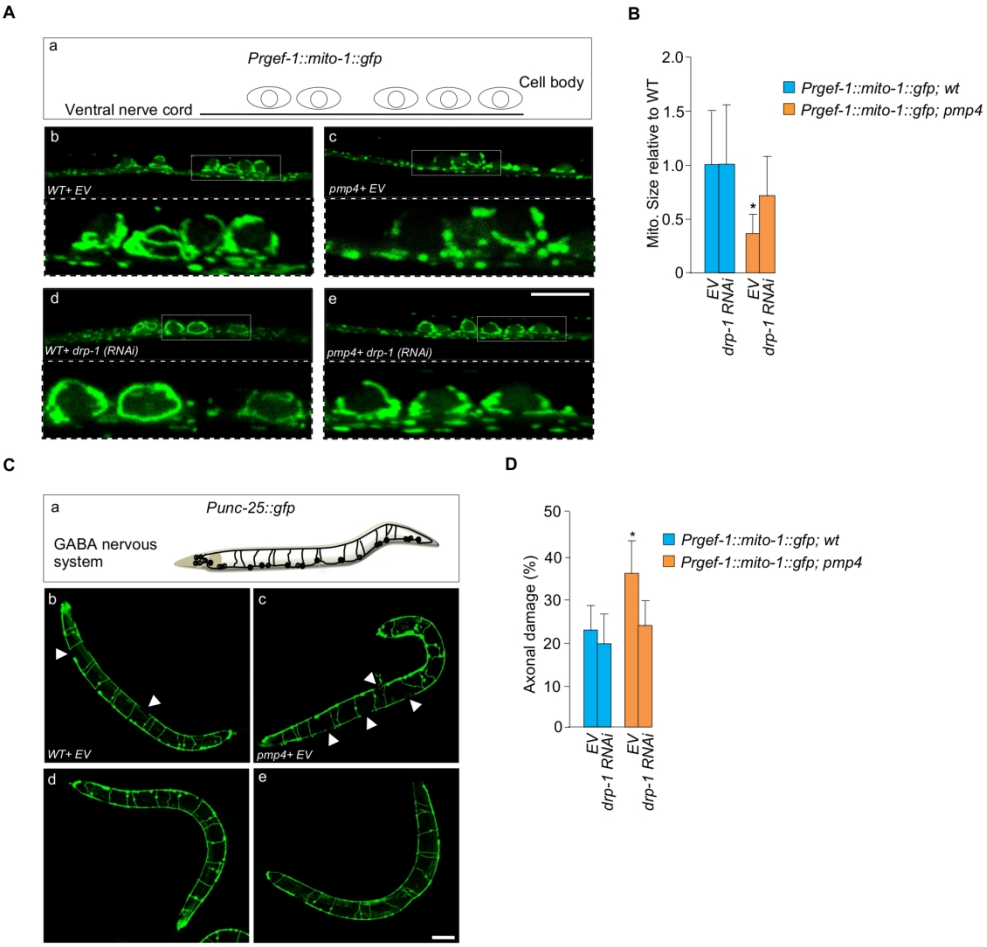

Figure 6. Inhibition of DRP1 improves mitochondrial morphology and axonal degeneration in an X-ALD worm model.

(A-D) Synchronized L1 worms at the indicated genotypes were treated with RNAi against drp-1 or empty vector control (EV). (A) (a) Schematic representation of neurons in the ventral nerve cord is shown in the upper panel. (b-e) Representative fluorescence images of a Pan-neuronal Prgef-1::mito-1::GFP transgene in (b) wild-type (WT), (c) pmp-4(ok396) worms, (d) wild-type (WT) worms treated with drp-1 siRNA, and (e) pmp-4(ok396) worms treated with drp-1 siRNA. Scale bar =10 μm. (B) Quantification of mitochondrial size of neuron cell bodies. (C) (a) Schematic representation of the C. elegans GABAergic nervous system. (b-e) Representative images of GABA neuron cell body processes in the ventral nerve cord and dorsally projecting commissures labeled with GFP in (b) juIs76 [Punc-25::gfp], (c) pmp-4(ok396); juIs76 [Punc-25::gfp], (d) juIs76 [Punc-25::gfp] treated with drp-1 RNAi, and (e) pmp-4(ok396); juIs76 [Punc-25::gfp] treated with drp-1 RNAi at the L4 stage. Commissural abnormalities and gaps in the dorsal and ventral cord are labeled with white arrows. Scale = 25 □m. (D) Quantification of the axonal defects. All values are expressed as the mean ± SD (between 20 and 25 cell bodies were analyzed per genotype and condition in B; between 30 and 40 animals were analyzed per genotype and condition in D; *P<0.05 and ***P<0.001, one-way ANOVA followed by Tukey's HSD post hoc test).

181x187mm (300 x 300 DPI)

Figure 7

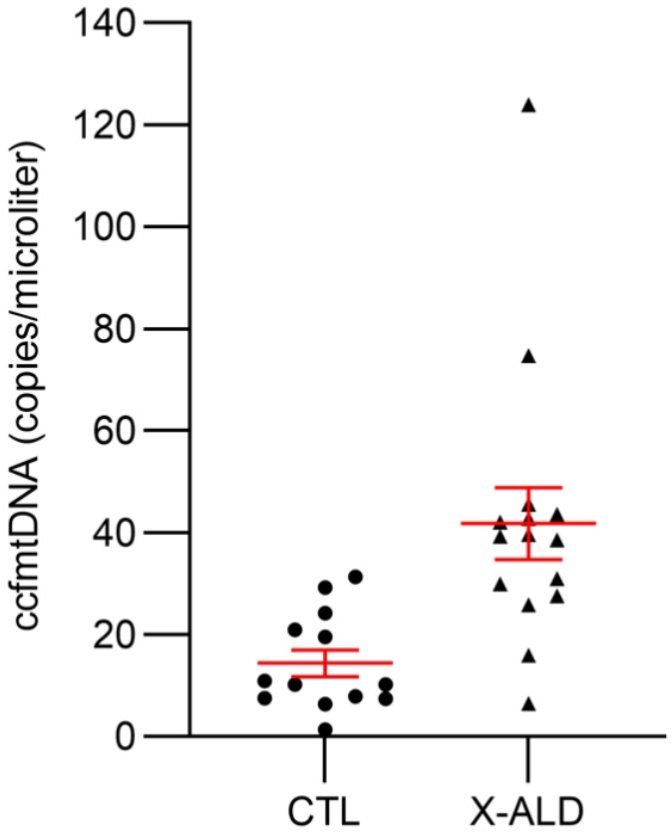

Figure 7. Cell-free circulating mitochondrial DNA (ccfmtDNA) is increased in X-ALD cerebrospinal fluid Quantification of ccfmtDNA in the CSF of AMN patients (n=15) and sex and age-matched controls (n=13). Values are expressed as the number of copies per microliter. mean ± SEM. ***P<0.001, two-tailed Mann–Whitney test.

64x85mm (300 x 300 DPI)

Supplementary Material

Supplementary Tables

Supplementary Table 1. C.elegans strains

Name	Source	Identifier
Wild type (WT)	CGC	N2
pmp-4(ok396) IV	CGC	RB675
juIs76 [Punc-25::gfp + lin-15(+)] II	CGC	CZ1200
muIs32 [Pmec-7::gfp + lin-15(+)] II	CGC	CF702
pmp-4(ok396) IV; juIs76 [Punc-25::gfp + lin-15(+)] II	[83]	EDC072
pmp-4(ok396) IV; muIs32 [Pmec-7::gfp + lin-15(+)] II	[83]	EDC067
Ex129 [Prgef-1::mito::gfp::(unc-54)3'UTR + rol-6(su1006)]	this study	EDC036
pmp-4(ok396) IV; Ex130 [Prgef-1::mito::gfp::(unc-54)3'UTR + rol-6(su1006)]	this study	EDC037

Supplementary Table 2. Primers and probes used for ddPCR

Name	Sequence (5'-3')	Amplicon length (bp)
ND1 forward ND1 reverse ND1 probe	CCCTAAAACCCG CCACATCT GAGCGATGGTGA GAGCTAAGGT 6-FAM/CCATCACCC/Zen/TCTA CATCACCGCCC/IABkFQ	69
ND4 forward ND4 reverse ND4 probe	CCATTCTCCTCCT ATCCCTCAAC CACAATCTGATG TTTTGGTTAAAC TATATTT	84

	HEX/CCGACATCA /Zen/TTACCGGGT TTTCCTCTTG/IAB kFQ	
B2M forward B2M reverse B2M probe	CACTGAAAAAGA TGAGTATGCC AACATTCCCTGA CAATCCC HEX/CCGTGTGAA /Zen/CCATGTGAC TTTGTC/IABkFQ	231
BAX forward BAX reverse BAX probe	CCAGGATCGAGC AGGGCGAA CACTCGCTCAGC TTCTTGGT HEX/CCCGAGCTG /Zen/GCCCTGGAC CCGGT/IABkFQ	93

Supplementary Figures

Supplementary Figure 1

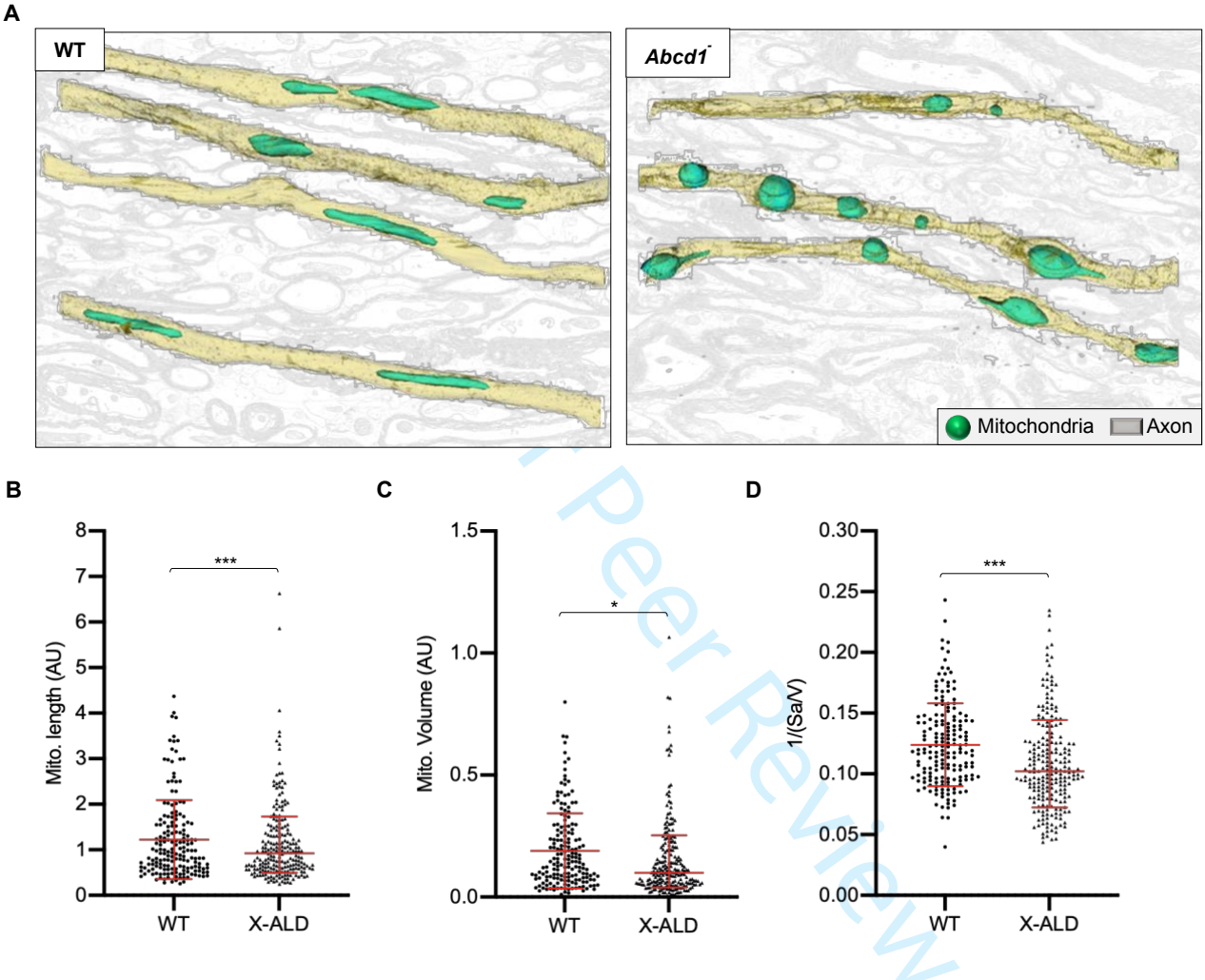

Supplementary Figure 2

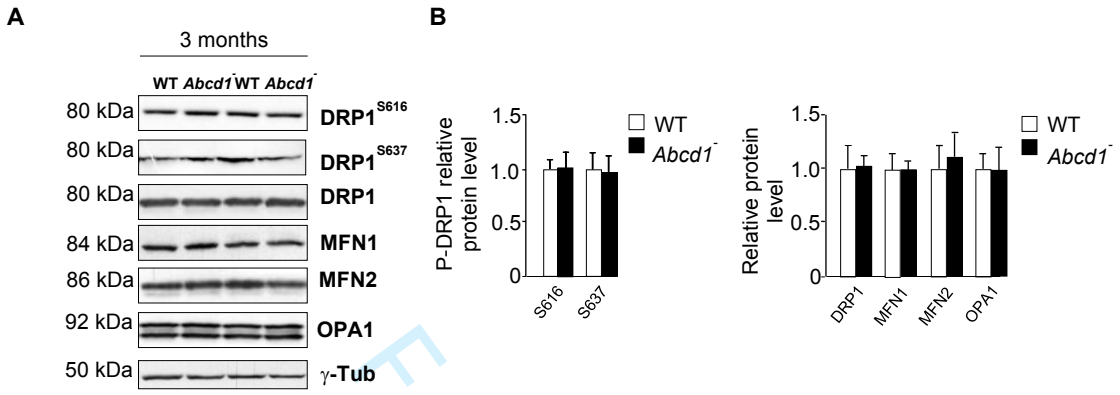

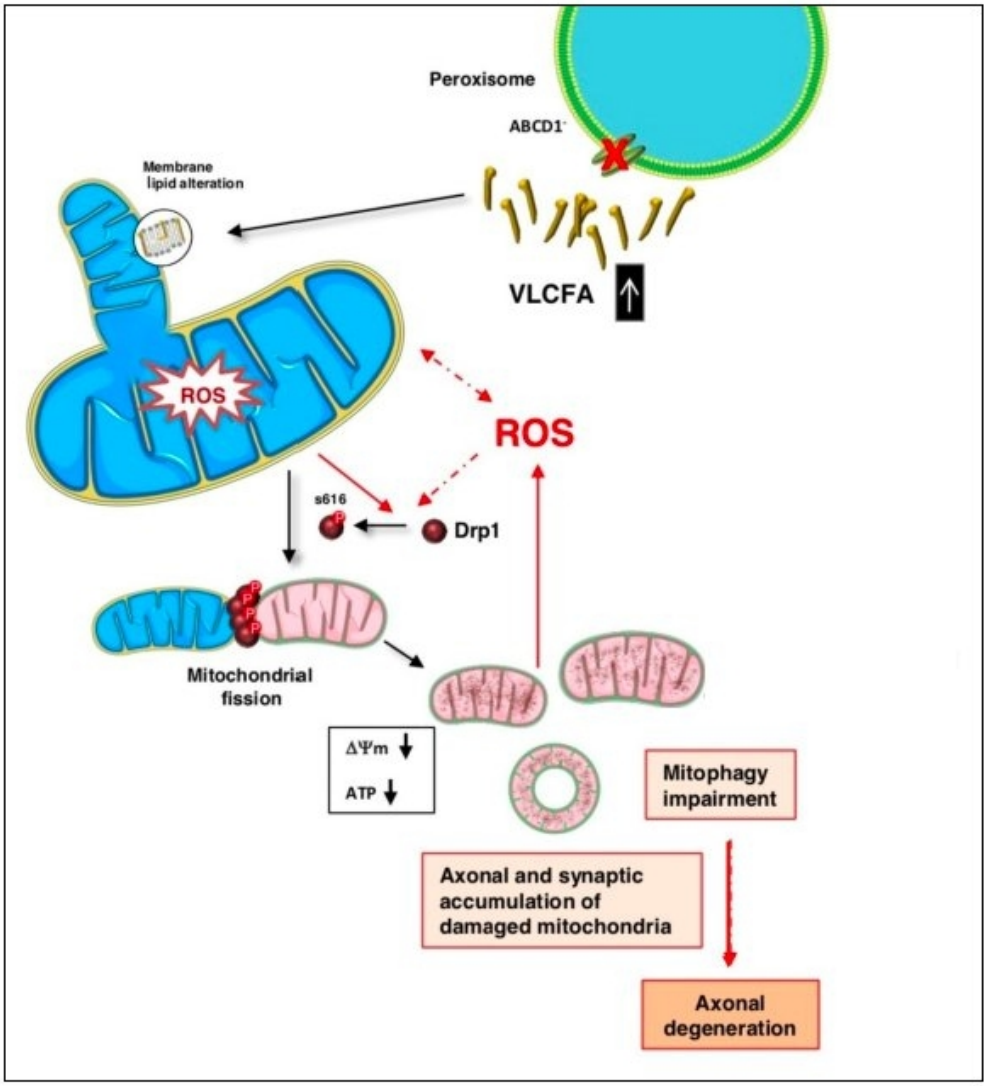

The role of mitochondrial dynamics in axonal degeneration in X-ALD.
Very long-chain fatty acid-induced redox imbalance triggers pro-fission DRP1S616 phosphorylation, leading to mitochondrial fragmentation and the formation of donut-shaped mitochondria. Dysfunctional mitochondria increase mitochondrial ROS production and oxidative damage, which further contribute to axonal degeneration in X-ALD.

207x228mm (72 x 72 DPI)

Reporting checklist for study using laboratory animals.

		Reporting Item	Page Number
Essential 10			
Study design	#1a	Give details of the groups being compared, including control groups. If no control group has been used, the rationale should be stated.	4 and 10
Study design	#1b	Give details of the experimental unit (e.g., a single animal, litter, or cage of animals).	4 and 10
Sample size	#2a	Specify the exact number of experimental units allocated to each group, and the total number in each experiment. Also indicate the total number of animals used.	30-31
Sample size	#2b	Explain how the sample size was decided. Provide details of any a priori sample size calculation, if done.	n/a
Inclusion and exclusion criteria	#3a	Describe any criteria used for including or excluding animals (or experimental units) during the experiment, and data points during the analysis. Specify if these criteria were established a priori. If no criteria were set, state this explicitly.	n/a
Inclusion and exclusion criteria	#3b	For each experimental group, report any animals, experimental units, or data points not included in the analysis and explain why. If there were no exclusions, state so.	n/a
Inclusion and exclusion criteria	#3c	For each analysis, report the exact value of n in each experimental group.	30-31
Randomisation	#4a	State whether randomisation was used to allocate experimental units to control and treatment groups. If done, provide the method used to generate the randomisation sequence.	n/a

Statistical methods	#7a	Provide details of the statistical methods used for each analysis, including software used.	11
Statistical methods	#7b	Describe any methods used to assess whether the data met the assumptions of the statistical approach, and what was done if the assumptions were not met.	11
Experimental animals	#8a	Provide species-appropriate details of the animals used, including species, strain and substrain, sex, age or developmental stage, and, if relevant, weight.	4 and 10 Supplementary Table 1
Experimental animals	#8b	Provide further relevant information on the provenance of animals, health/immune status, genetic modification status, genotype, and any previous procedures.	4
Experimental procedures	#9a	For each experimental group, including controls, describe the procedures in enough detail to allow others to replicate what was done, how it was done, and what was used.	4 and 10
Experimental procedures	#9b	Timing and frequency of procedures	4 and 10
Experimental procedures	#9c	Where procedures were carried out (including detail of any acclimatisation periods).	4 and 10
Results	#10a	For each experiment conducted, including independent replications, report summary/descriptive statistics for each experimental group, with a measure of variability where applicable (e.g., mean and SD, or median and range).	Fig.3 And Fig. 6
Results	#10b	If applicable, for each experiment conducted, including independent replications, report the effect size with a confidence interval.	n/a

Recommended set

Abstract	#11	Provide an accurate summary of the research objectives, animal species, strain and sex, key methods, principal findings, and study conclusions.	1
Background	#12a	Include sufficient scientific background to understand the rationale and context for the study, and explain the experimental approach.	3-4
Background	#12b	Explain how the animal species and model used address the scientific objectives and, where appropriate, the relevance to human biology.	3-4
Objectives	#13	Clearly describe the research question, research objectives and, where appropriate, specific hypotheses being tested.	3-4
Ethical statement	#14	Provide the name of the ethical review committee or equivalent that has approved the use of animals in this study and any relevant licence or protocol numbers (if applicable). If ethical approval was not sought or granted, provide a justification.	5
Housing and husbandry	#15	Provide details of housing and husbandry conditions, including any environmental enrichment.	n/a
Animal care and monitoring	#16a	Describe any interventions or steps taken in the experimental protocols to reduce pain, suffering, and distress.	n/a
Animal care and monitoring	#16b	Report any expected or unexpected adverse events.	n/a
Animal care and monitoring	#16c	Describe the humane endpoints established for the study, the signs that were monitored, and the frequency of monitoring. If the study did not set humane endpoints, state this.	n/a
Interpretation/scientific implications	#17a	Interpret the results, taking into account the study objectives and hypotheses, current theory, and other relevant studies in the literature.	18-20
Interpretation/scientific implications	#17b	Comment on the study limitations, including potential sources of bias, limitations of the animal model, and imprecision associated with the results.	n/a

Generalisability/translation	#18	Comment on whether, and how, the findings of this study are likely to generalise to other species or experimental conditions, including any relevance to human biology (where appropriate).	12 and 16-17
Protocol registration	#19	Provide a statement indicating whether a protocol (including the research question, key design features, and analysis plan) was prepared before the study, and if and where this protocol was registered.	n/a
Data access	#20	Provide a statement describing if and where study data are available.	11
Declaration of interests	#21a	Declare any potential conflicts of interest, including financial and nonfinancial. If none exist, this should be stated.	21
Declaration of interests	#21b	List all funding sources (including grant identifier) and the role of the funder(s) in the design, analysis, and reporting of the study.	21